

Abstract

We perform a geomagnetic event simulation using a newly developed magnetohydrodynamic with adaptively embedded particle-in-cell (MHD-AEPIC) model. We have developed effective criteria to identify reconnection sites in the magnetotail and cover them with the PIC model. The MHD-AEPIC simulation results are compared with Hall MHD and ideal MHD simulations to study the impacts of kinetic reconnection at multiple physical scales. At the global scale, the three models produce very similar SYM-H and SuperMag Electrojet (SME) indexes, which indicates that the global magnetic field configurations from the three models are very close to each other. We also compare the ionospheric solver results and all three models generate similar polar cap potentials and field aligned currents. At the mesoscale we compare the simulations with in situ Geotail observations in the tail. All three models produce reasonable agreement with the Geotail observations. At the kinetic scales, the MHD-AEPIC simulation can produce a crescent shape distribution of the electron velocity space at the electron diffusion region which agrees very well with MMS observations near a tail reconnection site. These electron scale kinetic features are not available in either the Hall MHD or ideal MHD models. Overall, the MHD-AEPIC model compares well with observations at all scales, it works robustly, and the computational cost is acceptable due to the adaptive adjustment of the PIC domain. It remains to be determined whether kinetic physics can play a more significant role in other types of events, including but not limited to substorms.

1 Introduction

A geomagnetic storm is a major disturbance of Earth's magnetosphere that occurs when a significant amount of energy is deposited into the geospace. The most widely used and successful simulation tools to study the geomagnetic storms are based on the magnetohydrodynamic (MHD) description, which is computationally feasible to solve. The first global MHD models were developed in the 1980s (LeBoeuf et al., 1981; Wu et al., 1981; Brecht et al., 1981, 1982). Later on, models with more advanced numerical algorithms have been developed, such as the Lyon-Fedder-Mobarry (LFM) (J. G. Lyon et al., 1986; J. Lyon et al., 2004), the OpenGGCM (Raeder et al., 1995, 1996) and the GUMICS (Grand Unified Magnetosphere Ionosphere Coupling Simulation) model (Janhunen, 1996).

In this paper, we use the University of Michigan's Space Weather Modeling Framework (SWMF (Tóth et al., 2012)) which also includes an MHD model, the Block Adaptive-Tree Solar-wind Roe-type Upwind Scheme (BATS-R-US) (Powell et al., 1999) as its global magnetosphere (GM) component. The SWMF has been applied to many storm event simulations (Tóth et al., 2007; Glocer et al., 2009; Haiducek et al., 2017), which is also been selected as the physics-based model at the Space Weather Prediction Center based on a thorough model comparison (Pulkkinen et al., 2013).

Magnetic reconnection plays a key role in the magnetosphere both at the dayside and in the tail. Despite all the successful applications MHD models have achieved, magnetic reconnection in the global MHD models relies on either Hall resistivity, or ad hoc anomalous resistivity, or simply numerical diffusion. The numerical diffusion plays an important role in both ideal and Hall MHD models because it is required to break the field lines. As we show in Appendix A, the reconnection rate remains finite when the grid resolution becomes finer. The Hall resistivity, although does not break the field lines that are frozen into the electron fluid, changes the structure of the reconnection region, which can lead to faster reconnection rate than ideal MHD (Birn et al., 2001). A current dependent anomalous resistivity has also been applied in MHD simulations (Raeder et al., 2001). However, none of these approximations truly describe the physical processes responsible for collisionless reconnection. It is very important to properly represent kinetic reconnection physics in a global simulation and check if it plays an important role in con-

66 tributing to the larger scale processes that eventually produce geomagnetic disturbances
 67 and space weather effects. Furthermore, the MHD approximation assumes that the dis-
 68 tribution functions of the ions and electrons are Maxwellian. Numerous observations sug-
 69 gest that this condition is violated especially near the magnetic reconnection sites (L.-
 70 J. Chen et al., 2016; Burch et al., 2016; Hwang et al., 2019; Lotekar et al., 2020).

71 The MHD with embedded Particle-In-Cell (MHD-EPIC) model (Daldorff et al., 2014)
 72 enables kinetic physics to be introduced into a global MHD model. The MHD-EPIC model
 73 has been successfully used to study the interaction between the Jovian wind and Ganymede’s
 74 magnetosphere (Tóth et al., 2016; Zhou et al., 2019, 2020); flux transfer events (FTEs)
 75 at the Earth’s dayside magnetopause (Y. Chen et al., 2017); Mars’ magnetotail dynam-
 76 ics (Y. Ma et al., 2018) and the dawn-dusk asymmetries discovered at the Mercury’s mag-
 77 netotail (Y. Chen et al., 2019). However, the iPIC3D (Markidis et al., 2010) code, which
 78 is the PIC model used in the MHD-EPIC simulations, can only run on a fixed Cartesian
 79 grid. The magnetotail (and the associated current sheet that contains the reconnection
 80 sites) typically exhibits a flapping motion (Tsutomu & Teruki, 1976; Volwerk et al., 2013)
 81 during a geomagnetic storms. Covering the whole domain of interest where reconnec-
 82 tion can occur in the magnetotail would require a very large PIC grid and would result
 83 in a massive computational cost. This may be feasible for a short simulation time (up
 84 to an hour or so) but geomagnetic storms that usually happen last for days, the com-
 85 putational cost would become prohibitive.

86 To tackle this problem, we have developed the MHD with Adaptively Embedded
 87 PIC (MHD-AEPIC) algorithm that allows smaller PIC region than MHD-EPIC, which
 88 saves computational resources. Shou et al. (2021) introduces this idea and verifies that
 89 covering part of the simulation domain with a dynamically moving PIC box gives the
 90 same solution as using larger fixed PIC domain, while running significantly faster. This
 91 justifies our effort to use an adaptive PIC region in the simulation. In this paper, we fur-
 92 ther improve this method and make it more flexible: 1. The size and shape of the ac-
 93 tive PIC regions can be adapted during the runtime; 2. The adaptation of the active PIC
 94 region is fully automatic. To realize the first feature, instead of iPIC3D, we use the FLEKS
 95 Flexible Exascale Kinetic Simulator (FLEKS) (Y. Chen et al., 2021) as the PIC model. FLEKS
 96 inherits all numerical algorithms from MHD-EPIC, and also accommodates an adaptive
 97 PIC grid that allows PIC cells to be turned on and off during the simulation. In addi-
 98 tion, FLEKS employs a particle splitting and merging scheme to improve the simulation
 99 efficiency and accuracy. FLEKS is described in more detail in Section 2.2.

100 We have developed a reliable and efficient algorithm to identify potential recon-
 101 nection sites in the magnetotail using three local criteria. The criteria are easy to com-
 102 pute and provide the information to the FLEKS code to adapt its grid to cover the re-
 103 connection sites. This newly developed MHD-AEPIC model is applied to simulate a mag-
 104 netic storm. The SWMF simulation involves BATSRUS, FLEKS, the ionosphere elec-
 105 trodynamics model RIM (Ridley et al., 2004) and the inner magnetosphere model RCM
 106 (Wolf et al., 1982; Toffoletto et al., 2003). This is the first simulation of a real event with
 107 kinetic reconnection physics in the magnetotail scaling from the global scales of the mag-
 108 netosphere to the electron scales near the reconnection sites.

109 In this paper, we employ the new model to simulate the magnetic storm of 2011-
 110 08-05. We cover the tail reconnection sites with the adaptive PIC model. We also per-
 111 form ideal MHD and Hall MHD simulations for comparison. All simulations are fully cou-
 112 pled with the inner magnetosphere and ionospheric electrodynamic models within the
 113 Space Weather Modeling Framework. We focus on the impact of using ideal MHD, Hall
 114 MHD and MHD-AEPIC physics on the dynamical processes in the magnetotail. To make
 115 the comparison straightforward, we use the ideal MHD model at the dayside in all three
 116 simulations.

117 The computational methods are described in Section 2, the demonstration of the
 118 adaptation feature and comparisons between models and observations are shown in Sec-
 119 tion 3 and we summarize in Section 4.

120 2 Methods

121 2.1 Global Magnetosphere Model: BATS-R-US

122 The Block-Adaptive Tree Solar-wind Roe-type Upwind Scheme (BATS-R-US) is
 123 used as the Global Magnetosphere (GM) model in our simulation. In the Hall MHD and
 124 MHD-AEPIC simulations in this paper, the Hall MHD equations (Tóth et al., 2008) are
 125 solved. The Hall term is handled with a semi-implicit scheme. The spatial discretiza-
 126 tion uses a 2nd order accurate TVD scheme with the Artificial Wind Riemann solver (Sokolov
 127 et al., 1999) and the Koren limiter (Koren, 1993) with $\beta = 1.2$. The hyperbolic clean-
 128 ing (Dedner et al., 2003) and eight-wave scheme (Powell et al., 1999) are used to keep
 129 the magnetic field approximately divergence-free.

130 The Hall MHD equations with a separate electron pressure equation are

$$\frac{\partial \rho}{\partial t} = -\nabla \cdot (\rho \mathbf{u}) \quad (1)$$

$$\frac{\partial(\rho \mathbf{u})}{\partial t} = -\nabla \cdot \left[\rho \mathbf{u} \mathbf{u} + (p + p_e) \bar{I} + \frac{B^2}{2\mu_0} \bar{I} - \frac{\mathbf{B}\mathbf{B}}{\mu_0} \right] \quad (2)$$

$$\frac{\partial e}{\partial t} = -\nabla \cdot \left[(\epsilon + p) \mathbf{u} + p_e \mathbf{u}_e + \mathbf{u}_e \cdot \left(\frac{B^2}{\mu_0} \bar{I} - \frac{\mathbf{B}\mathbf{B}}{\mu_0} \right) \right] + p_e \nabla \cdot \mathbf{u}_e \quad (3)$$

$$\frac{\partial \mathbf{B}}{\partial t} = -\nabla \times \left[-\mathbf{u}_e \times \mathbf{B} - \frac{\nabla p_e}{ne} \right] \quad (4)$$

$$\frac{\partial p_e}{\partial t} = -\nabla \cdot (p_e \mathbf{u}_e) - (\gamma - 1) p_e \nabla \cdot \mathbf{u}_e \quad (5)$$

131 where \bar{I} is the identity matrix, ρ is the mass density, \mathbf{u} is the plasma bulk velocity, \mathbf{B}
 132 is the magnetic field, p_e is the electron pressure, p is the ion pressure and $\mathbf{j} = \nabla \times \mathbf{B} / \mu_0$
 133 is the current density. The Hall velocity and electron bulk velocity are defined as

$$\mathbf{v}_H = -\frac{\mathbf{j}}{ne} = -\frac{M_i}{e} \frac{\mathbf{j}}{\rho} \quad (6)$$

$$\mathbf{u}_e = \mathbf{u} + \mathbf{v}_H \quad (7)$$

134 where $n = \rho / M_i$ is the number density, M_i is the ion mass, and e is the elementary charge.
 135 The total energy density is defined as

$$e = \epsilon + \frac{B^2}{2\mu_0} = \frac{1}{2} \rho \mathbf{u}^2 + \frac{p}{\gamma - 1} + \frac{B^2}{2\mu_0} \quad (8)$$

136 where $\epsilon = \rho \mathbf{u}^2 / 2 + p / (\gamma - 1)$ is the hydrodynamic energy density of the ions and $\gamma =$
 137 $5/3$ is the adiabatic index. The thermal energy density of the electrons is $\epsilon_e = p_e / (\gamma -$
 138 $1)$. We note that the $e + \epsilon_e$ is conserved both analytically and numerically as the non-
 139 conservative source terms $\pm p_e \nabla \cdot \mathbf{u}$ in equations (3) and (5) cancel out. Apart from $(\rho, \mathbf{u}, \mathbf{B}, p, p_e)$,
 140 other variables are derived quantities.

141 The continuity equation (1), momentum equation (2), energy equation (3) and elec-
 142 tron pressure equation (5) are solved with an explicit time stepping scheme. In the in-
 143 duction equation (4), the convection term $\mathbf{u} \times \mathbf{B}$ and pressure gradient term $\nabla p_e / ne$
 144 are solved using an explicit scheme, while the Hall term $\mathbf{v}_H \times \mathbf{B}$ is advanced with an
 145 implicit scheme. The Hall MHD equations introduce whistler mode wave, which has a
 146 characteristic wave speed inversely proportional to the wavelength. The shortest wave-
 147 length that exists in a numerical simulation is proportional to the cell size Δx , so the
 148 fastest whistler wave speed in a simulation is proportional to $1/\Delta x$. The time step in

149 a fully explicit scheme is limited by the Courant-Friedrichs-Lewy (CFL) condition: $\Delta t <$
 150 $\Delta x/c_{\max}$, where c_{\max} is the fastest wave speed, which leads to a time step proportional
 151 to $1/(\Delta x)^2$. We use a semi-implicit scheme (Tóth et al., 2012) to handle the stiff Hall
 152 term in the induction equation, so that the time step of the explicit part is only limited
 153 by the fast magnetosonic wave speed instead of the whistler speed.

154 A three-dimensional block-adaptive Cartesian grid is used to cover the entire compu-
 155 tational domain $-224 R_E < x < 32 R_E$, $-128 R_E < y, z < 128 R_E$ in GSM coor-
 156 dinates. The Hall effect is restricted to $x \in [-100 R_E, 20 R_E]$, $|y| < 30 R_E$ and $|z| <$
 157 $20 R_E$ box region excluding a sphere of radius $3R_E$ centered at the Earth to speed up
 158 the simulation. Outside this region the Hall effect is neglected by setting $\mathbf{v}_H = 0$. In
 159 the magnetosphere, the smallest ion inertial length $d_i = c/\omega_{pi}$ is about $1/20 R_E$ in the
 160 tail lobe region, which is already extremely difficult for a 3-D global MHD model to re-
 161 solve, let alone the PIC code. Tóth et al. (2017) introduced a scaling approach which
 162 scales up the kinetic length by artificially increasing ion mass per charge by a scaling fac-
 163 tor. The scaling does not change the fluid variables, such as density, pressure, velocity,
 164 IMF and dipole field, and the global structure of the magnetosphere will not change sig-
 165 nificantly as long as the scaled up ion inertial length is much smaller than the global scales.
 166 In this paper, we use a factor of 16, which satisfies this condition. On the other hand,
 167 with the ion inertial length scaled up by 16 times, we don't need an extremely fine grid
 168 to resolve it. We set the grid cell size in the magnetotail to $\Delta x = 1/4 R_E$, which is about
 169 4 times smaller than the scaled up ion inertial length. About fourteen million cells are
 170 used in total. For MHD model simulations, we also apply $1/8 R_E$ grid resolution in the
 171 tail: $x \in [-60R_E, -10R_E]$ and $|y|, |z| < 10 R_E$. This increases the total number of cells
 172 to about twenty three millions, which is still feasible to do (but would be too expensive
 173 for MHD-AEPIC model). Comparing the simulation results with $1/4 R_E$ and $1/8 R_E$ res-
 174 olutions in the tail allows us to look into the role of numerical resistivity.

175 At the inner boundary $r = 2.5R_E$, the density is calculated by the empirical for-
 176 mula $\rho_{\text{inner}} = (28 + 0.1\text{CPCP}) \text{ amu/cm}^3$, where CPCP is the average of the northern
 177 and southern cross polar cap potentials measured in keV. This boundary condition has
 178 been used successfully in previous geomagnetic storm simulations (Pulkkinen et al., 2013).
 179 The pressure and the magnetic field \mathbf{B}_1 (excluding dipole field) have zero gradient at the
 180 inner boundary, while the radial velocity is set to zero and the tangential velocity is cal-
 181 culated from the corotation and the $\mathbf{E} \times \mathbf{B}$ drift, where the electric field \mathbf{E} is provided
 182 by the Ridley Ionosphere Model (RIM) (Ridley et al., 2004).

183 2.2 Particle-in-cell Model: FLEKS

184 The FLExible Exascale Kinetic Simulator (FLEKS) (Y. Chen et al., 2021) is used
 185 as the particle-in-cell (PIC) model (PC component in the SWMF) to resolve kinetic physics.
 186 FLEKS uses the same two-way coupling method as MHD-EPIC (Daldorff et al., 2014)
 187 and the Gauss's law satisfying energy-conserving semi-implicit method (GL-ECSIM) (Y. Chen
 188 & Tóth, 2019) for the PIC solver. To enable the adaptation in MHD-AEPIC, FLEKS
 189 introduces an adaptive grid that allows changing simulation region dynamically. Figure
 190 1 shows a schematic plot of the adaptive grid. We choose $\Delta x = 1/4R_E$ to be the PIC
 191 grid resolution so that the scaled $d_i/\Delta x \sim 4$. The ion inertial length inside the mag-
 192 netosphere is described in Subsection 2.1. The ion-electron mass ratio is set to 100 in
 193 this simulation so that the electron skin depth $d_e = 0.1d_i$. Li et al. (2019) perform 2-
 194 D PIC simulations using different ion-electron mass ratios and conclude that features
 195 like reconnection rate and magnetic energy conversion are similar in simulations using
 196 different ion-electron mass ratios. Although the grid is not refined to resolve the elec-
 197 tron scale, in the PIC model the electron particles can resolve sub-grid scale physics un-
 198 der the influence of the electromagnetic field that is resolved on the ion scale. Y. Chen
 199 and Tóth (2019) show that the semi-implicit PIC model can reproduce the most impor-
 200 tant ion scale features of magnetic reconnection with $d_i/\Delta x \sim 4$. The selected reso-

201 lution balances between the computational cost and the requirement of resolving kinetic
 202 scales.

203 FLEKS provides a particle merging and splitting scheme to maintain the number
 204 of particles per cell within bounds. Merging particles in a cell with high number of par-
 205 ticles can improve load-balancing and speed up simulation, while splitting particles in
 206 a cell with few particles can reduce noise and improve accuracy for the PIC simulation.
 207 This feature is very useful keeping the number of particles per cell about uniform dur-
 208 ing a long geomagnetic storm simulation.

209 2.3 Selection Criteria of PIC Regions

210 As described in the previous section, FLEKS allows patches to be turned on and
 211 off during the simulation. To make the active PIC patches only cover the regions of in-
 212 terest, where magnetic reconnection is happening or will be triggered soon, the MHD
 213 model should locate these regions and pass this information to FLEKS. Finding the lo-
 214 cations of magnetic reconnection sites can be done in various ways including tracing field
 215 lines (Glocer et al., 2016). For sake of efficiency and generality, here we use local crite-
 216 ria based on the local MHD solution only.

217 Magnetic reconnection usually happens in current sheets where the current den-
 218 sity j is strong and the magnetic field B is weak. In particular, the field B_{\perp} that is per-
 219 pendicular to the current \mathbf{j} should be close to zero, while the guide field parallel to the
 220 current can be non-zero. We define the following non-dimensional relation as our first
 221 criterion

$$\frac{J\Delta x}{B_{\perp} + \varepsilon} = \frac{J^2\Delta x}{|\mathbf{J} \times \mathbf{B}| + J\varepsilon} > c_1 \quad (9)$$

222 where $\mathbf{J} = \mu_0\mathbf{j} = \nabla \times \mathbf{B}$ and ε is a small dimensional constant in units of the mag-
 223 netic field introduced to avoid dividing by zero. We use $\varepsilon = 1$ nT in our simulations pre-
 224 sented here, which is much smaller than the typical magnetic field intensity in the tail
 225 current sheet. Δx is the local cell size that is used in calculating the curl of the mag-
 226 netic field, so that $J\Delta x$ is the jump of the transverse magnetic field between neighbor-
 227 ing grid cells. We set $c_1 = 0.8$ in this work to select the cells that are close to the re-
 228 connection sites.

229 While criterion (9) works quite well in general, we sometimes find that it selects
 230 the axis of flux ropes, or O-lines, in addition to X-lines, especially if ε is very small. Re-
 231 connection does not occur at O-lines, so we developed a second criterion that distinguishes
 232 X- and O-lines based on the divergence of the magnetic field curvature vector:

$$[\nabla \cdot (\mathbf{b} \cdot \nabla \mathbf{b})](\Delta x)^2 > c_2 \quad (10)$$

233 where $\mathbf{b} = \mathbf{B}/|\mathbf{B}|$ is a unit vector along the magnetic field. We use $c_2 = -0.1$ to iden-
 234 tify X-lines where the curvature vectors point away from the X-line, so their divergence
 235 is positive.

236 The above two criteria are identifying potential magnetic reconnection sites through
 237 local plasma properties in a general scenario. However, current sheets in the solar wind
 238 can also satisfy those two criteria. To make the selection more selective, we need to in-
 239 troduce a third criterion to exclude the volume outside the magnetosphere. Observations
 240 show that specific entropy is two orders of magnitude larger in the magnetosphere than
 241 in the magnetosheath (X. Ma & Otto, 2014) and our simulations properly reproduce these
 242 properties. Here we use the specific entropy as the third criterion:

$$\frac{p}{\rho^{\gamma}} > c_3 \quad (11)$$

243 where p is the plasma thermal pressure, ρ is the plasma density, and $\gamma = 5/3$ is the ra-
 244 tio of the specific heats (Birn et al., 2006, 2009). Different from the c_1 and c_2 introduced
 245 above, this criterion is dimensional and we use the threshold value $c_3 = 0.02$ nPa/cm^{-3 γ} .

246 The three criteria combined can identify X-lines in the magnetotail well. To make
 247 the active PIC region large enough around the X-lines, we flag all patches where all three
 248 criteria are met, and then activate all patches within a distance L_x , L_y and L_z from these
 249 flagged patches in the x , y and z directions, respectively. The extension in each direc-
 250 tion enables the PIC model to cover a buffer area outside the reconnection sites. This
 251 buffer ensures that the velocity distribution of ions and electrons at the boundary of the
 252 PIC region can be well approximated with a drifting Maxwellian distribution, which re-
 253 sults in a consistent coupling between the MHD model. We use $L_x = 4R_E$ and $L_y =$
 254 $L_z = 2R_E$ in this work.

255 Each MPI process of BATS-R-US calculates the above criteria on their respective
 256 sub-domains overlapping with the PIC grid and activate the patches of the PIC grid where
 257 all 3 criteria are satisfied. Then the processors collect the information: a PIC patch is
 258 activated if any of the BATS-R-US processes activated it. Since the status of all PIC patches
 259 (on/off) is stored in each MPI processor of BATS-R-US, using the default logical array
 260 would consume a lot of memory. To reduce the memory use, the status is stored by a
 261 single bit, which is 32 times smaller than the size of the default logical variable in For-
 262 tran. The information is conveniently collected with the bitwise "or" operator `MPI BOR`
 263 used in the `MPI_ALLREDUCE` call.

264 **2.4 Ionospheric Electrodynamics Model: RIM**

265 The Ionospheric Electrodynamics (IE) is simulated by the Ridley Ionosphere Model
 266 (RIM) (Ridley et al., 2004) that solves a Poisson-type equation for the electric poten-
 267 tial on a 2-D spherical grid. In this work, the grid resolution is set to 2° in both longi-
 268 tude and latitude directions. The lower latitude boundary is at 10° where the electric
 269 potential is set to zero.

270 The BATS-R-US and RIM models are two-way coupled every 5 seconds. To cal-
 271 culate the Poisson-type equation, RIM obtains the field-aligned currents (FAC) calcu-
 272 lated at $3R_E$ from the BATS-R-US model and maps them down to its grid. The F10.7
 273 flux is also an input parameter of RIM that is used together with the FAC to calculate
 274 the particle precipitation and conductances based on an empirical model. The electric
 275 field calculated by the RIM is mapped back to the inner boundary of BATS-R-US to ob-
 276 tain the $\mathbf{E} \times \mathbf{B}/B^2$ velocity for its inner boundary condition. The cross polar cap po-
 277 tentials (CPCP, (the difference of the maximum and minimum potentials in the two hemi-
 278 spheres) are also sent to BATS-R-US to set the density at the inner boundary.

279 **2.5 Inner Magnetosphere Model: RCM**

280 The Inner Magnetosphere (IM) is modeled by the Rice Convection Model (RCM)
 281 (Wolf et al., 1982; Toffoletto et al., 2003). The standard RCM settings are used, includ-
 282 ing an exponential decay term with a 10-hour e-folding rate. The decay term makes the
 283 Dst index recover better after strong storms. As a component of the SWMF geospace
 284 model, RCM is used in all simulations presented in this paper.

285 The RCM model is one-way coupled with RIM and two-way coupled with BATS-
 286 R-US every 10 seconds. RIM sends the electric potential to RCM, where it is used to
 287 advect the field lines with the $\mathbf{E} \times \mathbf{B}/B^2$ drift. In the two-way coupling between BATS-
 288 R-US and RCM, BATS-R-US identifies the closed field line regions and calculates field
 289 volume integrals of pressure and density (De Zeeuw et al., 2004). The integrated pres-
 290 sure and density are applied to RCM as the outer boundary condition with the assump-
 291 tion of 90% H^+ and 10% O^+ number density composition. From RCM to BATS-R-US,
 292 the GM grid cell centers are traced to the RCM boundary along the magnetic field lines
 293 (De Zeeuw et al., 2004) and the BATS-R-US pressure and density are pushed towards
 294 the RCM values with a 20 s relaxation time.

3 3D Global Simulation with Kinetic Physics in the Magnetotail

3.1 Simulation Setup

We apply the MHD-AEPIC method to the geomagnetic storm event of Aug. 6. 2011 with an observed minimum Dst -126 nT. Previous modeling works show frequent flapping motion of the magnetotail current sheet during the storm (Tsutomu & Teruki, 1976; Volwerk et al., 2013), so the adaptive embedding feature is perfect for only covering the current sheet during the simulation. We start our simulation at 2011-08-05 15:00:00 and end it at 2011-08-06 07:00:00. This time range covers the main phase and the early recovering phase of the storm when the largest geomagnetic impact happens. The solar wind inputs are shown in Figure 2. First the BATS-R-US and RIM models are run to reach a quasi-steady state after 50k iteration steps using local time stepping. Figure 3 shows the plasma density along with the different refinement level boundaries of the AMR grid in the meridional plane for the steady state solution. Then the SWMF is switched to a time-accurate mode with FLEKS and RCM models turned on. Y. Chen et al. (2017) and Zhou et al. (2020) study the dayside reconnection at Earth and Ganymede by putting PIC regions at the magnetopause. They also compare the results with Hall MHD and conclude that the two models generate similar global features, such as flux rope formation and reconnection rate. In this paper, we only put PIC regions in the magnetotail, in order to control variants. The dayside reconnection is modeled by the ideal MHD. The computational domain of FLEKS is determined by the selection criteria introduced above. For sake of comparison, we also conduct two other simulations without FLEKS: one with Hall MHD model and the other with ideal MHD model.

3.2 PIC Region Adaptation

In this subsection, we highlight the utility and efficiency of the adaptive embedding scheme. Figure 4 illustrates how the PIC region is changing over the simulation. Panels (a)-(f) are snapshots from six different times. The color contours show the j_y component of the current density on the meridional plane to show the magnetospheric current system. Boundaries of the active PIC region are shown by the gray isosurface. Snapshots 4 (a) and (b) are taken before the sudden commencement of the storm. At this time, the IMF B_z is pointing northward and the solar wind speed is about 400 km/s. From the isosurface plot, the PIC region is covering the tail current sheet tilting southward. In Figure 4 (b), the tail current sheet is kinked and the PIC region adjusts its shape to accommodate the tail current sheet. Snapshots 4 (c)-(f) are taken after the sudden commencement of the storm. Here we observe a much compressed magnetosphere as well as an enhanced current density. In the last two snapshots, the tail current sheet is tilting northward and it is well covered by the PIC region. From the snapshots, we can conclude that the PIC region selection criteria work well in identifying the tail current sheet, which can make the PIC region accommodate with the flapping motion of the magnetotail. The translucent red line in Figure 4 (g) shows the volume of the active PIC region recorded every second from the simulation, while the solid red line is the volume smoothed over every minute. The Dst index is also presented in the background for reference. The volume of the PIC region increases after the sudden commencement and starts dropping in the recovering phase. This reflects that the tail current system intensity is related to the solar wind condition. Notice that the volume is less than $16,000 R_E^3$ for the entire storm simulation, which is only about 11.2% of the large PIC box extending from $-100R_E$ to $-10R_E$ in the x direction and $-20R_E$ to $20R_E$ in the y and z directions. This confirms that the MHD-AEPIC method saves substantial amount of computational resources.

3.3 Global Scale: Geomagnetic Indexes and Ionospheric Quantities

To evaluate the models' performance at the global scale, we use the SYM-H and SME as evaluation metrics. The SYM-H index approximates the symmetric portion of

345 the northward component of the magnetic field near the equator based on measurements
 346 at six ground magnetometer stations. This index characterizes the strength of the ring
 347 current (Ganushkina et al., 2017) and it is an indicator of storm activity. The SYM-H
 348 data with a 1-minute cadence is downloaded from NASA OMNIWeb Data Service. The
 349 SuperMAG electrojet (SME) index is an indicator of substorms and auroral power (Newell
 350 & Gjerloev, 2011). SME utilizes more than 100 ground magnetometer stations at geo-
 351 magnetic latitudes between $+40^\circ$ and $+80^\circ$, which resolves the large and extreme events
 352 more effectively than the traditional Auroral Electrojets (AE) index (Davis & Sugiura,
 353 1966; Bergin et al., 2020).

354 In our model, the simulated SYM-H is calculated by evaluating the Biot-Savart in-
 355 tegral at the center of the Earth from all currents in the simulation domain. Calculat-
 356 ing SME is more complicated: the magnetic field disturbances are calculated at the po-
 357 sitions of the 100+ ground magnetometer stations and the simulated SME is obtained
 358 following the SuperMAG procedure. From Figure 5, the MHD-AEPIC produces geomag-
 359 netic indexes close to the other two MHD models. The SYM-H plot shows that the ini-
 360 tial, main and recovery phases of the storm event are reproduced by all three models re-
 361asonably well. However, the models cannot reproduce the lowest SYM-H values that cor-
 362respond to the strongest observed geomagnetic perturbations. This feature can also be
 363observed in the SME plots: all three models produce increased auroral electrojets, how-
 364ever the second and third enhancements are weaker than the observed values. For MHD
 365model simulations, the root mean square errors (RMSE) of SYM-H and SME are not
 366changing much from $1/4 R_E$ to $1/8 R_E$ grid resolutions as shown in the figure 5. This
 367means that the numerical diffusion is not the major reason for the similarity of global
 368indexes generated from the three models, which demonstrates that the numerical diffu-
 369sion effect is converged to some extent on $1/4 R_E$ grid resolution in the tail. Fine grid
 370resolution towards $0.1 R_E$ is also applied in simulations using the LFM model (Wiltberger
 371et al., 2015; Merkin et al., 2019) and the authors demonstrate that the reconnection will
 372not be significantly suppressed if the grid resolution is further increased.

373 Apart from the global indexes such as SYM-H and SME, it is also important to com-
 374pare the amount of energy that the solar wind and interplanetary magnetic field (IMF)
 375transfer to Earth’s magnetosphere-ionosphere system through direct driving. The cross
 376polar cap potential (CPCP) is an indicator of this energy transfer process (Troshichev
 377et al., 1988, 1996). The CPCP is not directly measured but can be derived from obser-
 378vations using the Assimilative Mapping of Ionospheric Electrodynamics (AMIE) (Richmond
 379& Kamide, 1988) technique or from the Defense Meteorological Satellite Program (DMSP)
 380measurements (Hairston et al., 1998). Another approach based on the Super Dual Au-
 381roral Radar Network (SuperDARN) observations (Ruohoniemi & Greenwald, 1998) usu-
 382ally underestimates the CPCP significantly. We opt to use the readily available Polar
 383Cap Index (PCI) from the OMNIWeb website and convert it into CPCP using the em-
 384pirical relationship derived by Ridley and Kihn (2004):

$$\text{CPCP}_{\text{North}} = 29.28 - 3.31 \sin(T + 1.49) + 17.81\text{PCLN} \quad (12)$$

385 where T is the month of the year normalized to 2π . The storm event in this paper is in
 386 August, so $T = (8 - 1) * 2\pi/12$. Gao (2012) showed that this formula provides good
 387 agreement with AMIE and DMSP based approaches. For the southern hemisphere, since
 388 there is no published empirical relationship between southern CPCP and PCI, we change
 389 the sign in front of the $\sin(T+1.49)$ term (expressing the seasonal dependence) in the
 390 formula:

$$\text{CPCP}_{\text{South}} = 29.28 + 3.31 \sin(T + 1.49) + 17.81\text{PCLS} \quad (13)$$

391 The simulated CPCP is defined as the difference between the maximum and the min-
 392 imum of the electric potential obtained from the RIM model for both hemispheres.

393 Figure 6 (a) shows the northern and southern cross polar cap potentials from the
 394 three models together with the CPCP derived from the PCI. In general, the results from

the three models are very close to each other and have good agreements with the PCI derived CPCP for both hemispheres. Notice that the PCI is derived from a single station for each hemisphere while the model calculates CPCP using the entire electric potential. The differences between the model output and CPCP could be because the PCI is not measuring the ionospheric dynamics for the entire polar region. We observe that the three models generate the most different CPCP results during the main phase of the storm event at around $t = 2011-08-05\ 22:00:00$. Figure 6 (b) shows the polar cap potential and radial component of the field aligned currents for both hemispheres. The structure of the electric potentials as well as the field aligned currents are very similar among the three models.

The geomagnetic indexes and ionospheric quantities demonstrate that introducing kinetic physics in the magnetotail does not change the global configuration of the simulated magnetosphere and ionosphere significantly relative to the ideal and Hall MHD simulations. It is to be seen if this trend persists for other storms, especially extreme events.

3.4 Mesoscale: Magnetotail Dynamics

During the storm event, the Geotail spacecraft was in the magnetotail at $x \approx -29 R_E$ crossing the equatorial plane and approaching to the meridional plane. Figure 7 shows the magnetic field and ion moments observed by Geotail and compares them with the ideal-MHD, Hall-MHD and MHD-AEPIC simulations. The MHD-AEPIC model shows a reasonable agreement with the Geotail number density observation before $t = 2011-08-06\ 00:00$, including the current sheet crossing event between $t = 2011-08-05\ 22:00$ and $t = 2011-08-05\ 23:00$ while the Hall-MHD model overestimates the ion number density substantially. However, all three models generate much higher number density than observed after $t = 2011-08-06\ 00:00$. None of the three models show perfect agreement with the magnetic field observations. The B_x component gives us information about which side of the current sheet the satellite is. The comparison plot shows that the virtual satellites in the simulations are all on the opposite side of the current sheet than Geotail before $t = 2011-08-05\ 22:00$. Between $t = 2011-08-05\ 23:00$ and $t = 2011-08-06\ 01:00$, Geotail is crossing the current sheet from the north side to the south side, and this is captured by all three models. However, the next current sheet crossing at around $t = 2011-08-06\ 01:30$ is not captured by MHD-AEPIC and ideal-MHD. The Hall-MHD simulation produces a similar structure but with a 30-minute time shift. The B_y and B_z components give information about flux rope structures. All three models provide good agreement with the observation in terms of overall field magnitude, while it is difficult to tell which one is better in capturing fine details. Geotail observed a B_z reversal along with a relatively strong core B_y at around $t = 2011-08-06\ 05:00$, which indicates a flux rope. A similar structure is produced by MHD-AEPIC with a 30-minute delay, while there is no similar signal from the ideal-MHD and Hall-MHD simulations. Geotail observed high ion speed around 1000 km/s at $t = 2011-08-06\ 02:00$ and $t = 2011-08-06\ 03:00$. The MHD-AEPIC model only generates around 500 km/s ion speeds. Although the ideal-MHD and Hall-MHD models can produce maximum ion speeds around 1000 km/s, they also generate large scale oscillations that are not present in the observations. Overall, introducing kinetic physics in the magnetotail did not improve plasma and magnetic features compared to the ideal MHD simulation at the mesoscale. The Hall MHD simulation, on the other hand, produces significantly more oscillations than observed in multiple time periods.

Since Geotail only observes along a single trajectory, it cannot provide insight into the full dynamics of the magnetotail. To compare the different models, we plot results on 2-D surfaces. Figure 8 shows the magnetosphere simulation results from three models at the same time 2011-08-05 19:40:00. Figure 8 (a1), (b1) and (c1) show the x component of the ion bulk velocity and magnetic field lines in the meridional plane ($-80 R_E < x < -5 R_E$ and $-20 R_E < z < 10 R_E$) from MHD-AEPIC, Hall MHD and ideal MHD

447 simulations, respectively. The global configurations of the magnetosphere share a lot of
 448 similarities but there are several differences as well. All three models give a southward
 449 tilted magnetotail that is compressed most in the z direction at around $x = -40R_E$
 450 as a result of the IMF structure. In terms of the reconnection feature, all three models
 451 generate X-lines in the tail current sheet at around $x = -20R_E$ and $z = -5R_E$. Di-
 452 verging reconnection ion jets are generated at the major X-line for all three models.

453 To analyze physical quantities in the current sheet better, we extract the quanti-
 454 ties along a surface where $B_x = 0$ and project this surface to the $x-y$ plane for plot-
 455 ting. The bottom row in Figure 8 shows the z coordinate of the center of the current sheet.
 456 The structure is similar as in the meridional plane plots: the current sheets are at $z \approx$
 457 0 near Earth and at $z \approx -15R_E$ at far tail for MHD-AEPIC and Hall MHD models,
 458 while $z \approx -12R_E$ for ideal MHD. Figure 8 (a2)-(c2) show the ion bulk flow speed on
 459 the current sheet surface. There are significant differences among the three models in
 460 the earthward ion flow structures. For ideal MHD, the earthward ion flow is distributed
 461 roughly symmetrically at $-3R_E < y < 3R_E$. The earthward ion jet generated by Hall
 462 MHD can only be observed on the dawn side at $-5R_E < y < 0$. The MHD-AEPIC
 463 simulation produces earthward ion jet both on the dawn and dusk sides. However, the
 464 ion jet on the dawn side is further away from the earth than the jets on the dusk side.
 465 Also, the earthward ion jets can be observed from $-5R_E$ to $7R_E$ in the y direction, which
 466 agrees with the observations that earthward flows are observed at a wide range of y val-
 467 ues (Angelopoulos et al., 1994).

468 Although the earthward ion flow from MHD-AEPIC is different from pure MHD
 469 models, the similar magnetic field structure and current sheet position indicate that these
 470 snapshots from different models represent the same physical state of the magnetosphere.
 471 Hence, it is valid to examine the flux rope features based on these results. As first pro-
 472 posed to be formed in the Earth's magnetotail (Schindler, 1974), magnetic flux ropes are
 473 reported to be closely related to magnetic reconnection by various observations and sim-
 474 ulations (Hones Jr et al., 1984; Slavin et al., 1989; Daughton et al., 2006; Markidis et
 475 al., 2013). The observational characteristics of the flux ropes are a pair of positive and
 476 negative B_z signatures with a core magnetic field B_y in between. Hence, we plot the B_z
 477 and $|B_y|$ components on the current sheet surface in Figure 8(a-c)(2-3). Panels (c3) and
 478 (c4) show only one flux rope at $-40R_E$ and there is no evidence indicating flux rope ex-
 479 ists at the near earth plasma sheet from $-40R_E$ to the Earth based on the ideal MHD
 480 model results. The Hall MHD and MHD-AEPIC give very different flux rope occurrence
 481 (Figure 8 (a-b)(3-4)) from ideal MHD. In addition to the moving directions of the flux
 482 ropes, the diameter of the flux ropes also varies: the earthward flux ropes are observed
 483 as smaller ones. This difference has been reported in a thorough analysis of Geotail ob-
 484 servations (Slavin et al., 2003). By examining the flux ropes as a mesoscale feature, we
 485 can conclude that by modeling the reconnection physics better, the MHD-AEPIC and
 486 Hall MHD simulations produce more flux ropes in the magnetotail than ideal MHD as
 487 well as distinguish two types of the flux ropes. However, there is no evidence support-
 488 ing that MHD-AEPIC can produce better mesoscale features than Hall MHD. This could
 489 be the case because the spatial scale of the flux ropes is much larger than the kinetic scale
 490 which PIC model is resolving.

491 Figure 9 shows different physical quantities near the reconnection X-line at the same
 492 time as Figure 8. Panel (a) shows the current density of the current sheet j_y , the out-
 493 of-plane magnetic field B_y and the ion bulk velocity U_{ix} from the ideal MHD model. The
 494 current sheet is smooth and narrow around the X-line. The simulation produces diverg-
 495 ing ion outflow as expected. There is no significant B_y near the reconnection site due
 496 to the lack of Hall physics in the ideal MHD model. Panel (b) shows the same quanti-
 497 ties as Panel (a) for the Hall MHD model. In addition, the bottom plot shows the elec-
 498 tron velocity in the x direction calculated from the ion bulk velocity and the Hall veloc-
 499 ity as $u_{ex} = u_{ix} - j_x/(ne)$. Different from the current sheet in the ideal MHD model,

500 the current sheet in the Hall MHD simulation breaks up at multiple locations. There are
 501 strong B_y signatures in the Hall MHD simulation as expected from Hall physics, although
 502 the presence of the non-uniform guide field somewhat distorts the classical quadrupolar
 503 structure. The diverging ion bulk flow is very similar to the diverging electron flow,
 504 because the j_x component of the current is weak. Panel (c) shows the same quantities
 505 as Panel (b) from the MHD-AEPIC model with an extra ion nongyrotropy measure $D_{ng,i}$.
 506 The current sheet in the MHD-AEPIC simulation also forms multiple flux ropes similar
 507 to the Hall MHD results. The MHD-AEPIC model also generates the Hall magnetic
 508 field B_y . The ion and electron velocities from the MHD-AEPIC show very clear inflow
 509 and outflow features that are quite different from the Hall MHD solution. While both
 510 ideal and Hall MHD assume isotropic pressures, the PIC simulation allows a general pres-
 511 sure tensor with anisotropy and even nongyrotropy (non-zero off-diagonal terms). Aunai
 512 et al. (2013) defines the nongyrotropy measure as

$$D_{ng} = 2 \frac{\sqrt{P_{12}^2 + P_{23}^2 + P_{13}^2}}{P_{11} + P_{22} + P_{33}} \quad (14)$$

513 Here P_{ij} are the pressure tensor components in the local magnetic field aligned coordi-
 514 nate system. The D_{ng} quantity produced by the MHD-AEPIC model shows that the ion
 515 nongyrotropy increases near the X-line. In conclusion, both Hall MHD and MHD-AEPIC
 516 generate more features than the ideal MHD model. The MHD-AEPIC and the Hall MHD
 517 models generate similar Hall magnetic field structures and current sheet features. The
 518 MHD-AEPIC model generates distinct ion and electron bulk flows, as well as the nongy-
 519 rotropic pressure distribution near the X-line.

520 3.5 Kinetic Scale: Electron Velocity Distribution Function

521 In this subsection, we will demonstrate that the kinetic physics at the reconnect-
 522 ion site is also properly captured by the MHD-AEPIC model. The magnetic reconnect-
 523 ion is regarded as one of the most fundamental physical processes to transfer energy from
 524 magnetic field to plasma. Since the launch of the Magnetospheric Multiscale (MMS) mis-
 525 sion (Burch et al., 2016), magnetic reconnection has been observed at the electron scale
 526 during multiple satellite crossings of the electron diffusion region (EDR) (Webster et al.,
 527 2018). The EDR encounters exhibit electron nongyrotropy, which can be recognized by
 528 a crescent-shaped electron distributions (Torbert et al., 2018).

529 Figure 10 compares the MHD-AEPIC simulation with MMS observations (Hwang
 530 et al., 2019). Panel (a) is a contour plot of ion bulk velocity in the meridional plane at
 531 $t = 2011-08-05 \ 23:20:00$. The ion jets, a clear signature of magnetic reconnection, are
 532 shown by the blue and red colors. The dashed white line near the X-line, which is ro-
 533 tated about 13.3° , is the L direction of the local reconnection coordinate system. We also
 534 found that the M axis is aligned with the y axis in GSM. So the LMN coordinate vec-
 535 tors for this reconnection event are $L = (0.972, 0, 0.233)$, $M = (0, 1, 0)$ and $N = (-0.233, 0, 0.972)$.
 536 The electron velocities are shown in the LMN coordinate system to allow a direct com-
 537 parison with the MMS observations. Panels (b) and (d) show the electron velocity dis-
 538 tribution functions (VDF) from the model and the MMS observation. The simulation
 539 VDF of the electrons is collected inside an ellipsoid region centered at $(-30.6, 0.5, -0.9) R_E$
 540 with principle semi-axes $(0.3, 2.5, 0.3) R_E$ in the (x, y, z) directions, respectively. The red
 541 circle in panel (a) labeled by B is the cross section of the ellipsoid with the meridional
 542 plane. The choice of the ellipsoid shape is based on panel (c) that shows where the MMS
 543 observations were taken with respect to the reconnection site according to Figure 2 by
 544 Hwang et al. (2019). The MMS3 observations of the electron VDF (Hwang et al., 2019)
 545 at the location $(-18.1, 7.30, 0.66) R_E$ are shown in panel (d). Although the simulation
 546 and observation are not from the same event and the EDR is not at the same position
 547 in GSM coordinates, the electron data is collected at a similar location relative to the
 548 X-line and the velocity components are all projected to the LMN coordinates (see pan-
 549 els (a) and (c)).

550 This suggests that we can directly compare the two VDF plots in panels (b) and
 551 (d), and they indeed agree very well. The agreement is not only qualitative, but in fact
 552 quantitative. Since the ion-electron mass ratio is 100, the simulated electron velocity is
 553 multiplied by $\sqrt{\frac{m_{i,\text{real}}}{m_{e,\text{real}}} / \frac{m_{i,\text{simulation}}}{m_{e,\text{simulation}}}} \approx \sqrt{18.36} \approx 4.28$ to be comparable with the obser-
 554 vations. In both panels the velocity distribution extends to $\pm 40,000$ km/s in the N di-
 555 rection and $(-40,000, +20,000)$ km/s in the M direction. A non-Maxwellian core dis-
 556 tribution can also be clearly identified in both panels at $-20,000$ km/s $< v_y < 10,000$ km/s
 557 and $|v_z| < 10,000$ km/s. In addition to the electron diffusion region, we also collected
 558 electrons inside two other ellipsoids at the inflow (labeled by A) and outflow (labeled by
 559 C) regions. The semi-axes of these two ellipsoids are the same as before while the cen-
 560 ters of the ellipsoids are $(-28.5, 1.5, 0.5) R_E$ and $(-33.0, 1.5, -1.0) R_E$ in the (x, y, z)
 561 directions, respectively. Panels (e) and (f) shows the electron VDF in $L - N$ and $L -$
 562 M coordinates, the distribution can be characterized as a bidirectional beam distribu-
 563 tion (Asano et al., 2008). The distribution functions at outflow region in panels (g) and
 564 (h) are almost circles with shifted centers indicating the direction of the bulk velocities.
 565 The distribution functions from the inflow and outflow also agree very well with the ex-
 566 isting theories (Pritchett, 2006; Egedal et al., 2010). Hence, we can conclude that an MHD-
 567 AEPIC global simulation can generate electron phase space distributions that are very
 568 close to the MMS observations, and reproduces the main features of reconnection physics
 569 even at the electron scales.

570 4 Conclusions and Discussions

571 In this paper, we introduced a newly developed magnetohydrodynamic with adap-
 572 tively embedded particle-in-cell (MHD-AEPIC) model. The MHD-AEPIC allows PIC
 573 grid cells to be turned on and off during the simulation based on the physical criteria
 574 provided. Different from the previous MHD-EPIC model, which requires a fixed Carte-
 575 sian box to cover the PIC region, the MHD-AEPIC model enables PIC regions moving
 576 with the reconnection sites to save computational resources substantially. During the main
 577 phase of the storm, from $t = 2011-08-06$ 00:05:00 to $t = 2011-08-06$ 02:54:00, when the
 578 volume of the PIC domain is about $12,000 R_E^3$. The relative timings are the following:
 579 72.72% of CPU time is used on FLEKS, 13.26% is for BATS-R-US and 10.35% is taken
 580 by the coupling between FLEKS and BATS-R-US. The rest 3.67% of CPU time is con-
 581 sumed by RIM, RCM and the overhead of the SWMF. For the entire 16-hour geomag-
 582 netic storm simulation, the total wall time is 256.29 hours on 5600 CPU cores.

583 We also introduced three physics-based criteria to identify the reconnection regions
 584 in the magnetotail. To demonstrate the feasibility of the MHD-AEPIC model, we have
 585 performed a geomagnetic storm event simulation with kinetic physics embedded for the
 586 first time. It remains to be determined whether kinetic physics can play a more impor-
 587 tant role in other events, including but not limited to substorms. The flapping motion
 588 of the magnetotail current sheet during the geomagnetic storm highlights the advantage
 589 of the adaptation feature of the MHD-AEPIC model.

590 We have also simulated the same event using Hall MHD and ideal MHD models
 591 and compared the three models at multiple physical scales. We examined the global scale
 592 features by comparing the SYM-H and SME indexes which reflect the equatorial and au-
 593 roral region disturbances, respectively. All three models properly capture the global scale
 594 disturbances such as the main phase of the storm or the increase of the auroral electro-
 595 jet. However, all three models fail to produce the strongest intensity for the geoin-
 596 dices. Hence no significant difference is found among the three different models at the global
 597 scale for this event. This indicates that the global magnetosphere configuration from the
 598 three models are very close, the kinetic model embedded in the magnetotail does not im-
 599 prove the global scale feature for this geomagnetic storm. If this trend persists for other
 600 storms, especially extreme events, is still to be investigated.

601 We analyze the mesoscale features by comparing the magnetic field components
602 and ion profiles between the Geotail observation and the simulations. All three models
603 show fairly good agreement with the Geotail observations, however, none of the three
604 models can match all features such as all the current sheet crossing or flux rope signa-
605 tures. The Hall MHD simulation shows more oscillations than observed during a few time
606 periods. In this storm event, MHD-AEPIC and ideal MHD models produce similar agree-
607 ment with the in-situ observations of Geotail.

608 In addition to comparing with the Geotail observations, we also compare the three
609 models with respect to flux rope structures in the current sheet. Only one major flux
610 rope can be observed from the ideal MHD simulation at the selected time, while Hall MHD
611 and MHD-AEPIC can produce flux ropes at a wider range in the dawn-dusk direction.
612 The difference of two types of the flux ropes: earth-ward with smaller spatial scale and
613 tail-ward with a larger spatial scale is also illustrated by the MHD-AEPIC simulations,
614 in agreement with several observations (Slavin et al., 2003).

615 The electron scale kinetic physics is well reproduced by the MHD-AEPIC model.
616 We collect electron macro-particle velocities at the same side of the electron diffusion re-
617 gion as the MMS3 satellite did (Hwang et al., 2019). The velocity distribution functions
618 show excellent agreement between the simulation and the MMS3 observation. This demon-
619 strates that MHD-AEPIC can properly produce the electron scale features within a sin-
620 gular self-consistent global model while simulating a complete geomagnetic storm event.
621 In this particular simulation, including the kinetic reconnection physics does not improve
622 agreement with observations at meso- and global scales. This suggests that in this storm
623 event, the magnetosphere is mostly driven by the external solar wind and interplanetary
624 magnetic field and not by the internal reconnection dynamics.

625 It is to be investigated if the kinetic physics can have a more pronounced influence
626 on the physical condition of the magnetosphere when the external drivers are relatively
627 constant. Another important question is to compare the impact of kinetic versus numer-
628 ical reconnection during extreme events. In addition to studying the Earth's magneto-
629 sphere, we also expect the novel MHD-AEPIC model will find its applications in vari-
630 ous collisionless plasma systems that form small regions where kinetic effects are impor-
631 tant inside a large spatial domain.

632 **Data Availability Statement**

633 The Geotail data is publicly available at Data ARchives and Transmission System
634 (DARTS) of Institute of Space and Astronautical Science (ISAS) (<https://darts.isas.jaxa.jp>).
635 The MMS observation plot is acquired with consent from Dr. K.-J. Hwang (jhwang@swri.edu).
636 The SWMF code (including BATS-R-US and FLEKS) is publicly available through the
637 csem.engin.umich.edu/tools/swmf web site after registration. The simulation output and
638 scripts used for generating figures in this paper can be obtained online ([https://doi.org/10.7302/xtvh-
639 tq17](https://doi.org/10.7302/xtvh-tq17)) through the University of Michigan's Deep Blue Data repository, which is specif-
640 ically designed for U-M researchers to share their research data and to ensure its long-
641 term viability.

642 **Acknowledgments**

643 We thank Dr. Qusai Al Shidi at the University of Michigan for the script calculating the
644 SME index using interpolated virtual magnetometer data from BATS-R-US. This work
645 was primarily supported by NSF PRE-EVENTS grant No. 1663800. We also acknowl-
646 edge support from the NASA DRIVE Center at the University of Michigan under grant
647 NASA 80NSSC20K0600. We acknowledge the use of computational resources provided
648 by an NSF LRAC allocation at the Texas Advanced Computing Center (TACC) at The
649 University of Texas at Austin.

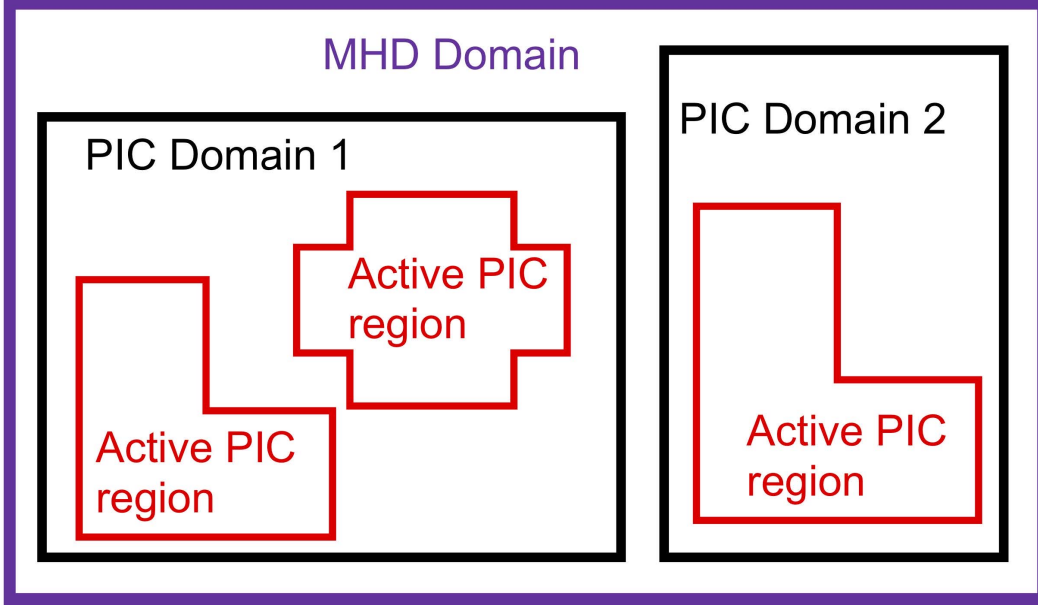


Figure 1. The schematic plot of the FLEKS adaptive grid. The red line boundary shows the flexibility of turning on and off the PIC patches during the simulation.

650 **Appendix A Reconnection due to numerical resistivity**

651 It is a common practice to rely on numerical resistivity to mimic reconnection physics
 652 in global ideal and Hall MHD simulations. Analytic solutions of ideal MHD obey the frozen-
 653 in condition: the magnetic flux through a surface co-moving with the plasma (i.e. the
 654 ion fluid) does not change. For Hall MHD the magnetic flux is frozen into the motion
 655 of the electron fluid. A consequence of the frozen-in condition is that if two plasma el-
 656 ements are connected by a field line, then they remain connected forever, which means
 657 that magnetic reconnection cannot take place.

658 In reality, and also in the kinetic PIC model, the electrons and ions can "detach"
 659 from the magnetic field lines in the ion and electron diffusion regions, respectively. In
 660 effect, this allows the magnetic field lines to reconnect inside the electron diffusion re-
 661 gion where the frozen in condition does not apply. The simplest mathematical descrip-
 662 tion of this process is adding an Ohmic resistive term $\eta \mathbf{j}$ into the induction equation:

$$\frac{\partial \mathbf{B}}{\partial t} = -\nabla \times [-\mathbf{u}_e \times \mathbf{B} + \eta \mathbf{j}] \quad (\text{A1})$$

663 For magnetic diffusivity $\eta' = \eta/\mu_0$ one can write this as

$$\frac{\partial \mathbf{B}}{\partial t} = -\nabla \times [-\mathbf{u}_e \times \mathbf{B}] - \nabla \times (\eta' \nabla \times \mathbf{B}) \quad (\text{A2})$$

664 where we used $\mathbf{j} = (1/\mu_0)\nabla \times \mathbf{B}$ and assumed that η is not constant in space in gen-
 665 eral. The usual argument in favor of using the ideal MHD model is that numerical re-
 666 sistivity will behave similarly to the diffusive term $\nabla \times (\eta' \nabla \times \mathbf{B})$ and indeed, numeri-
 667 cal experiments show that magnetic reconnection remains a robust feature of ideal MHD
 668 simulations. On the other hand, one would expect numerical diffusion to go to zero with
 669 increased grid resolution, which implies that reconnection should disappear from a well-
 670 resolved solution. In this appendix, we take a closer look at resolving this contradiction
 671 for 1D geometry and provide arguments for 3D geometry.

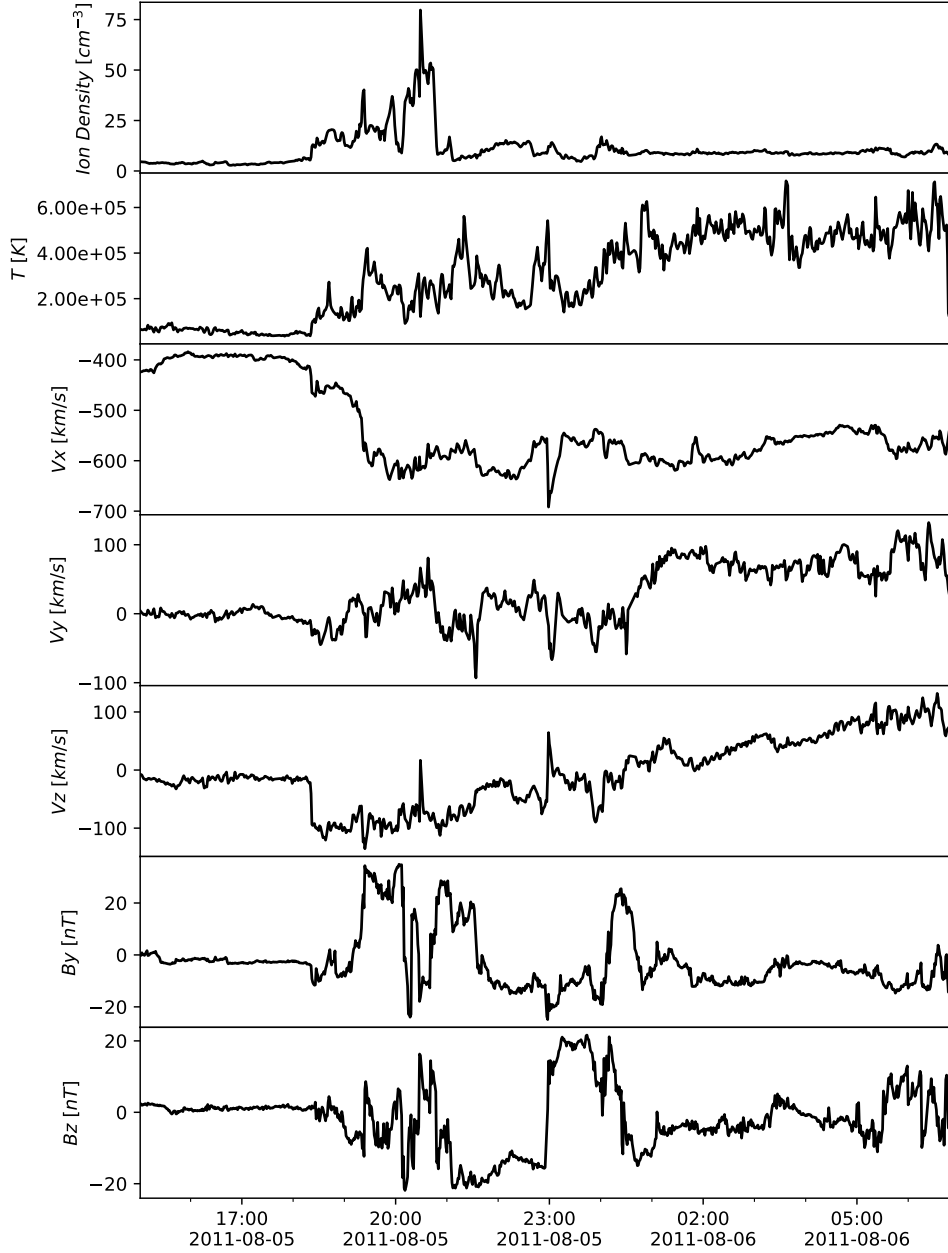


Figure 2. The solar wind bulk plasma and interplanetary magnetic field input in Geocentric Solar Magnetospheric coordinates (from top panel to the bottom: plasma density, plasma temperature, x, y and z components of the plasma flow velocity, y and z components of the magnetic field) for the simulation in this paper. The x -component of the magnetic field is set to be 0. The solar wind data is obtained from the ACE spacecraft observation and propagated to the bow shock position (Pulkkinen et al., 2013).

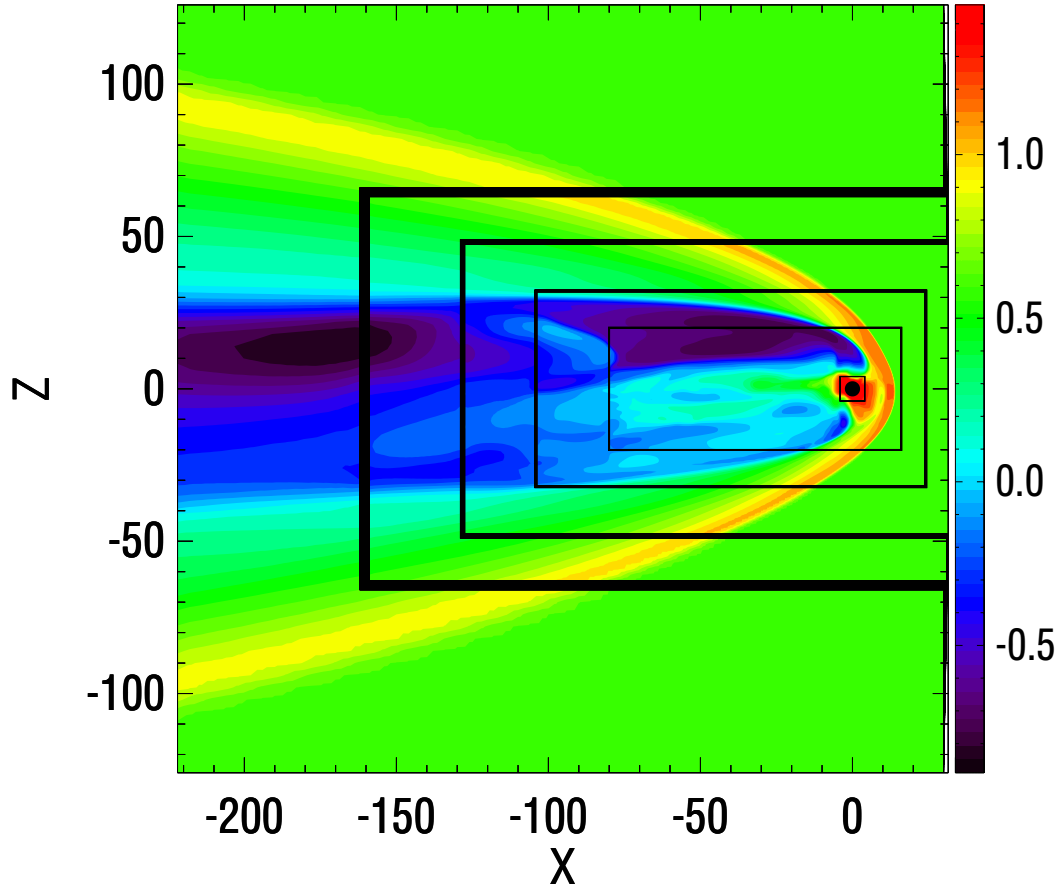


Figure 3. The meridional plane of the simulation domain. The color contour shows the plasma density of the steady state on a logarithmic scale. The black lines show the boundaries between different refinement levels. The refinement ratio between two adjacent levels is 2. The grid resolution near Earth is $1/8 R_E$ it is $1/4 R_E$ on the dayside and the magnetotail out to $x > -80 R_E$.

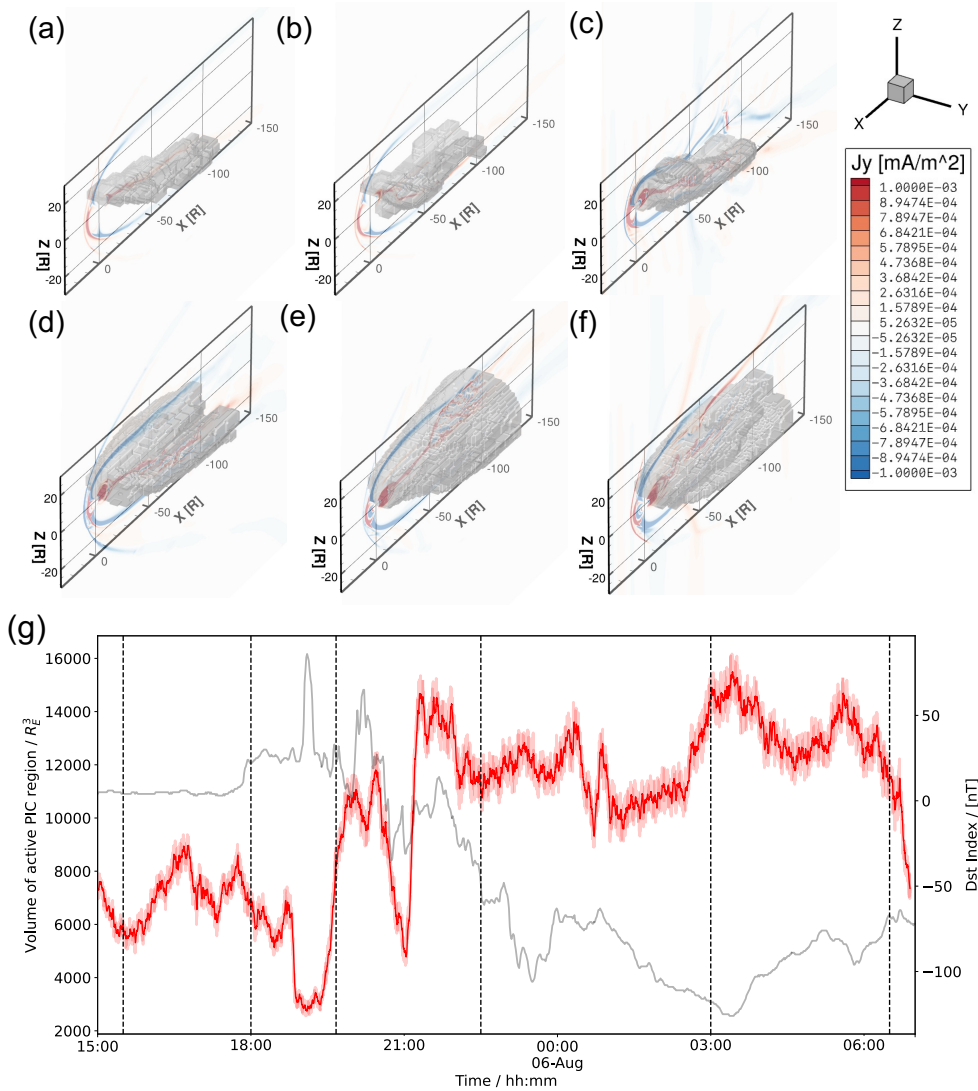


Figure 4. (a-f) Demonstration of PIC region adaptation during the simulation. The contour plot of j_y in the meridional plane is showing the general condition of the magnetospheric current system. The active PIC region boundary is shown by a gray isosurface. (g) Time evolution of the active PIC region volume. The translucent red line is the output every second and the solid red is the output smoothed every minute. The Dst index is plotted as a gray line for reference. The six vertical dashed lines correspond to the times of the snapshots (a)-(f), respectively.

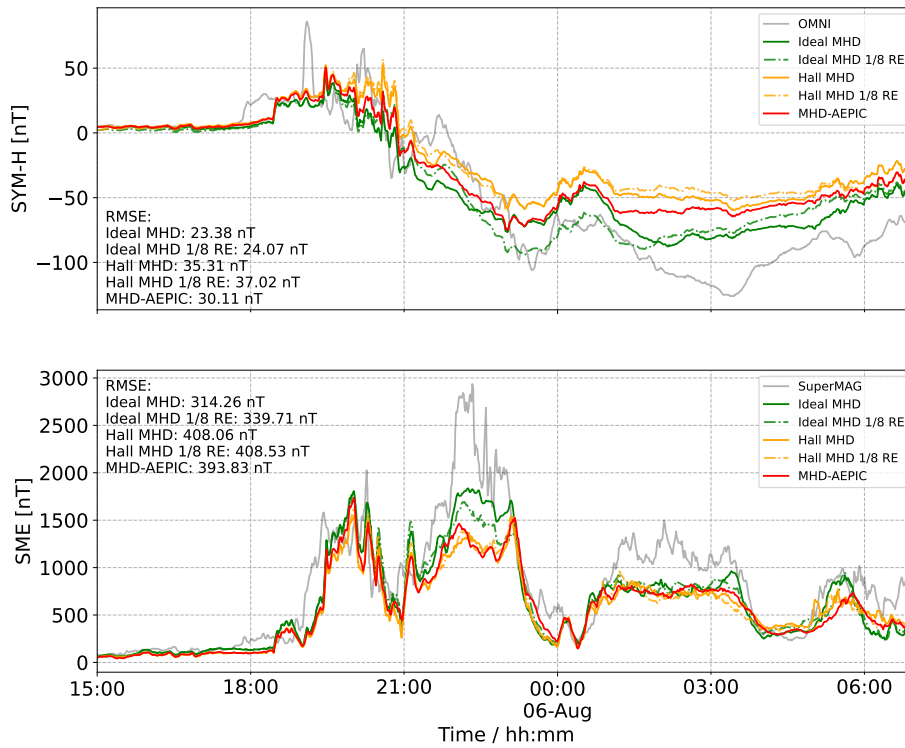


Figure 5. Aug. 6 2011 storm. Colored lines show the SYM-H and SuperMAG electrojet (SME) indexes from five simulations from three different models and the gray line corresponds to the observed indexes. The root mean squared error between the simulated indexes and observations are also presented.

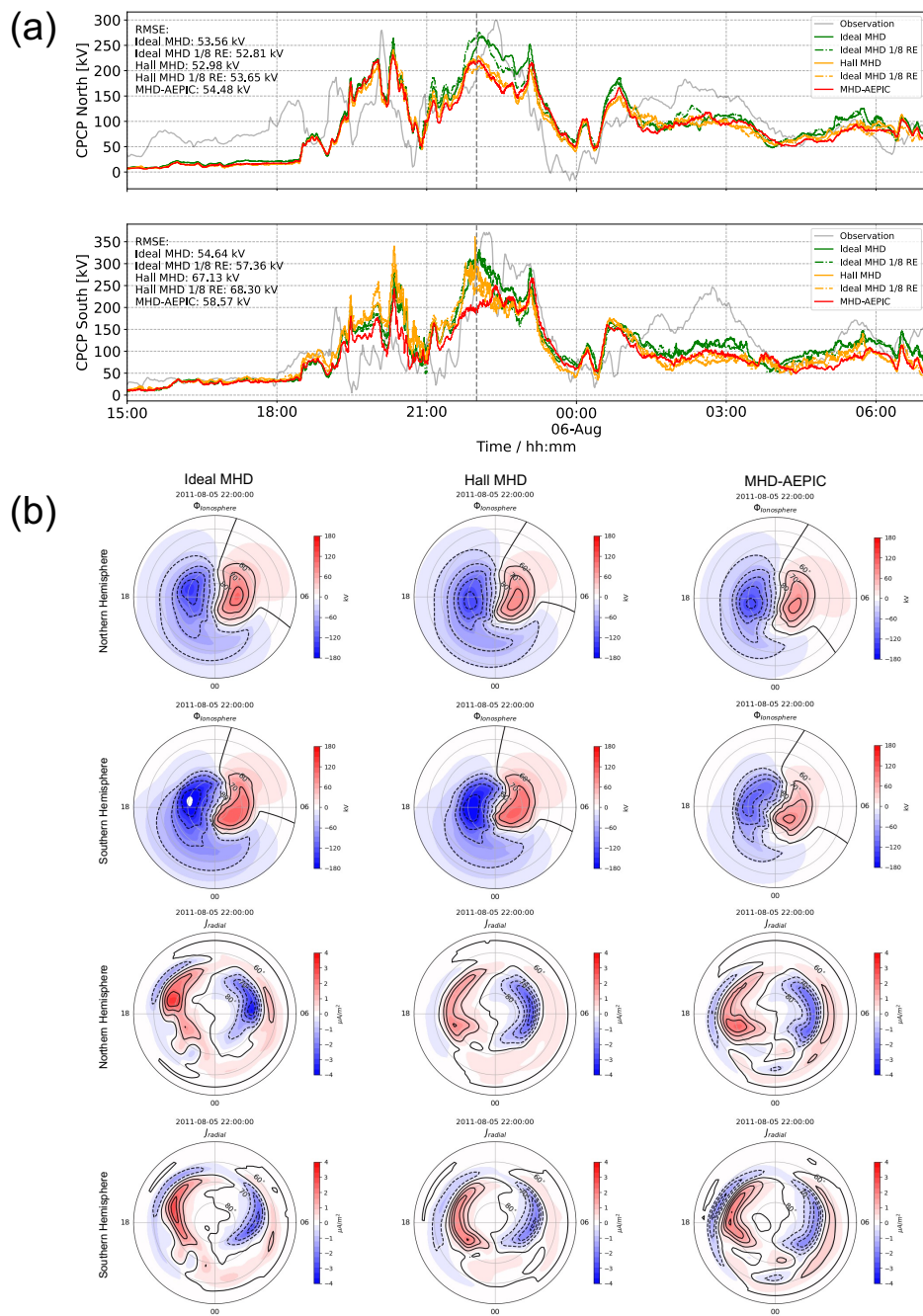


Figure 6. (a) The northern and southern cross polar cap potentials (CPCP) of the Aug. 6 2011 storm. Colored lines are model outputs, the gray line is the CPCP estimated (Ridley & Kihn, 2004) from the observed Polar Cap Index. The root mean squared error between the simulated indexes and observations are also presented. (b) The northern and southern electric potentials and the radial current from the three models at 2011-08-05 22:00:00 (marked with a vertical dashed line in panel (a)).

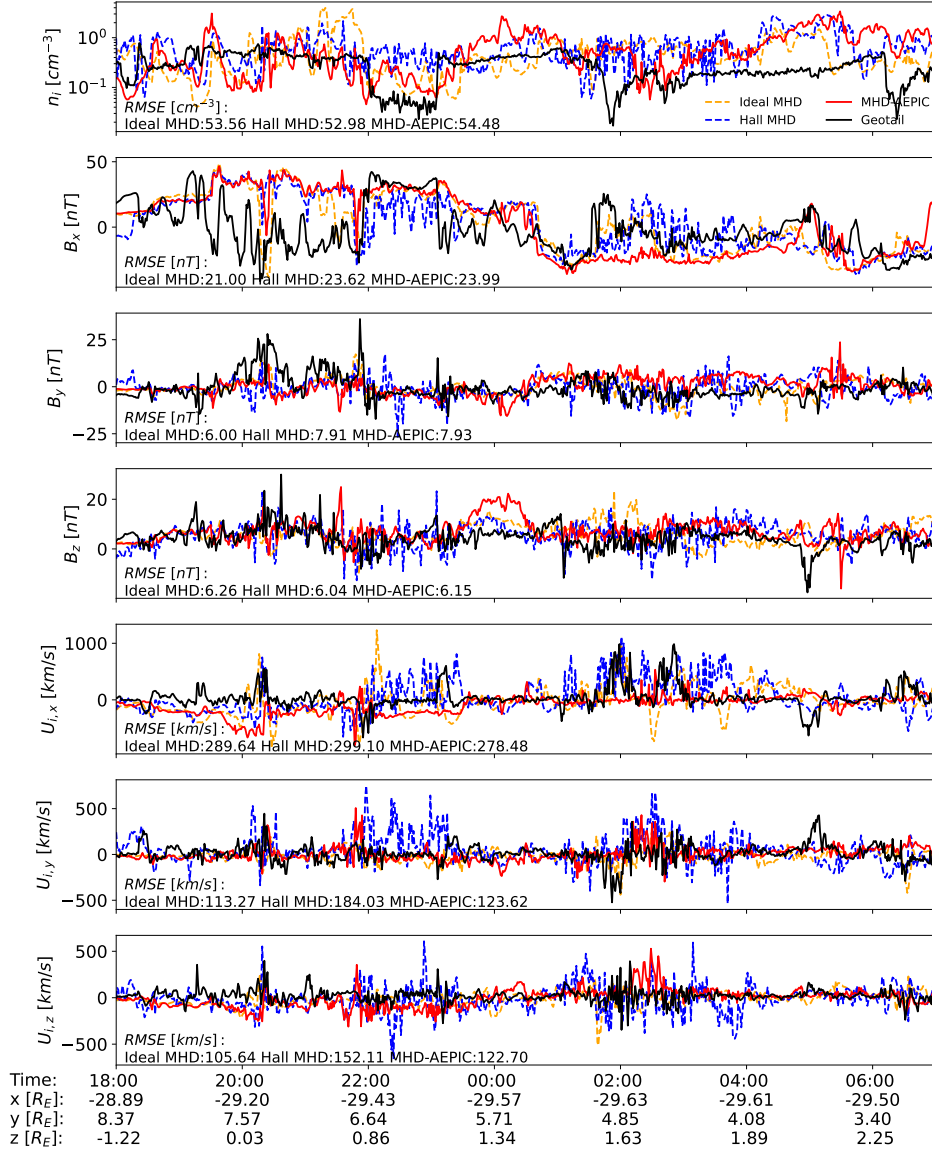


Figure 7. The ion density, magnetic field components and the ion velocity components observed by the Geotail spacecraft and the SWMF ideal MHD, Hall MHD and MHD-AEPIC simulations. The root mean squared error between the model outputs and observations are presented. The time interval shown starts from $t = 2011-08-05$ 18:00:00 right before the sudden commencement to $t = 2011-08-06$ 00:07:00 at the beginning of the recovery phase of the geomagnetic storm. The bottom X axis shows the GSE coordinates of the spacecraft at various times.

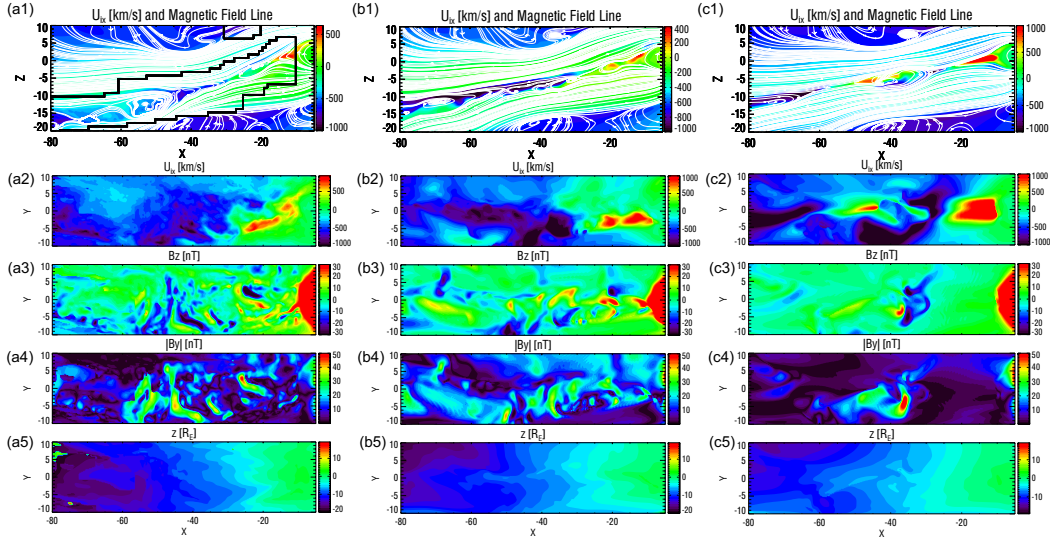


Figure 8. (a1) The x component of the ion bulk velocity $u_{i,x}$ and magnetic field lines on the meridional plane from the MHD-AEPIC simulation. The black line shows the boundary of the active PIC region. (a2) $u_{i,x}$ on the current sheet surface projected on the x - y plane. (a3) The contour plot of the B_z on the current sheet surface, color saturated at ± 30 nT. (a4) The absolute value of B_y on the current sheet surface. A pair of positive and negative B_z along with a core B_y indicates a flux rope structure. (a5) The z coordinate of the current sheet surface in the unit of R_E . (b1)-(b5) are same quantities from the Hall MHD and (c1)-(c5) are from the ideal MHD simulation. All snapshots are taken at the same time 2011-08-05 19:40:00.

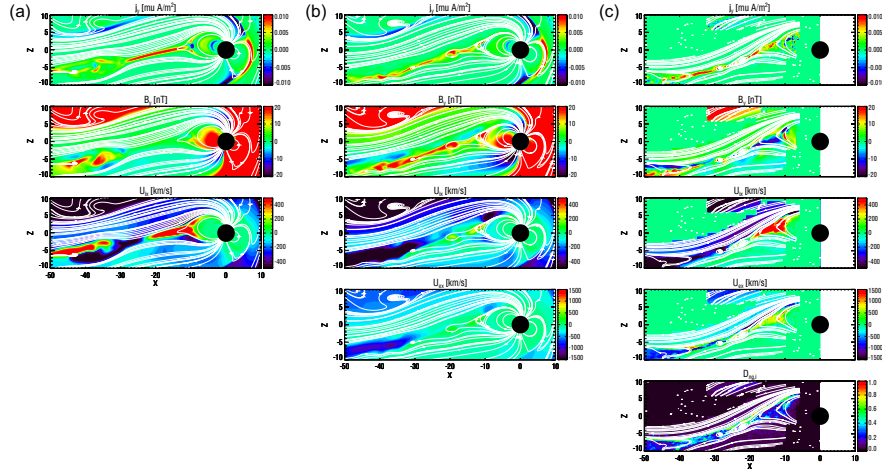


Figure 9. (a) The current density j_y , out-of-plane magnetic field B_y and ion bulk velocity in the x direction U_{ix} from the ideal MHD model near the reconnection X-line. (b) Same physical quantities as panel (a) from the Hall MHD model with an extra electron bulk velocity in the x direction U_{ex} calculated from the current. (c) Same physical quantities as panel (b) from the MHD-AEPIC model with an extra ion nongyrotropy measure $D_{ng,i}$ defined by Aunai et al. (2013). Only the data from the active PIC region is shown in column (c) identified by the area covered with magnetic field lines. All snapshots are taken at the same time 2011-08-05 19:40:00.

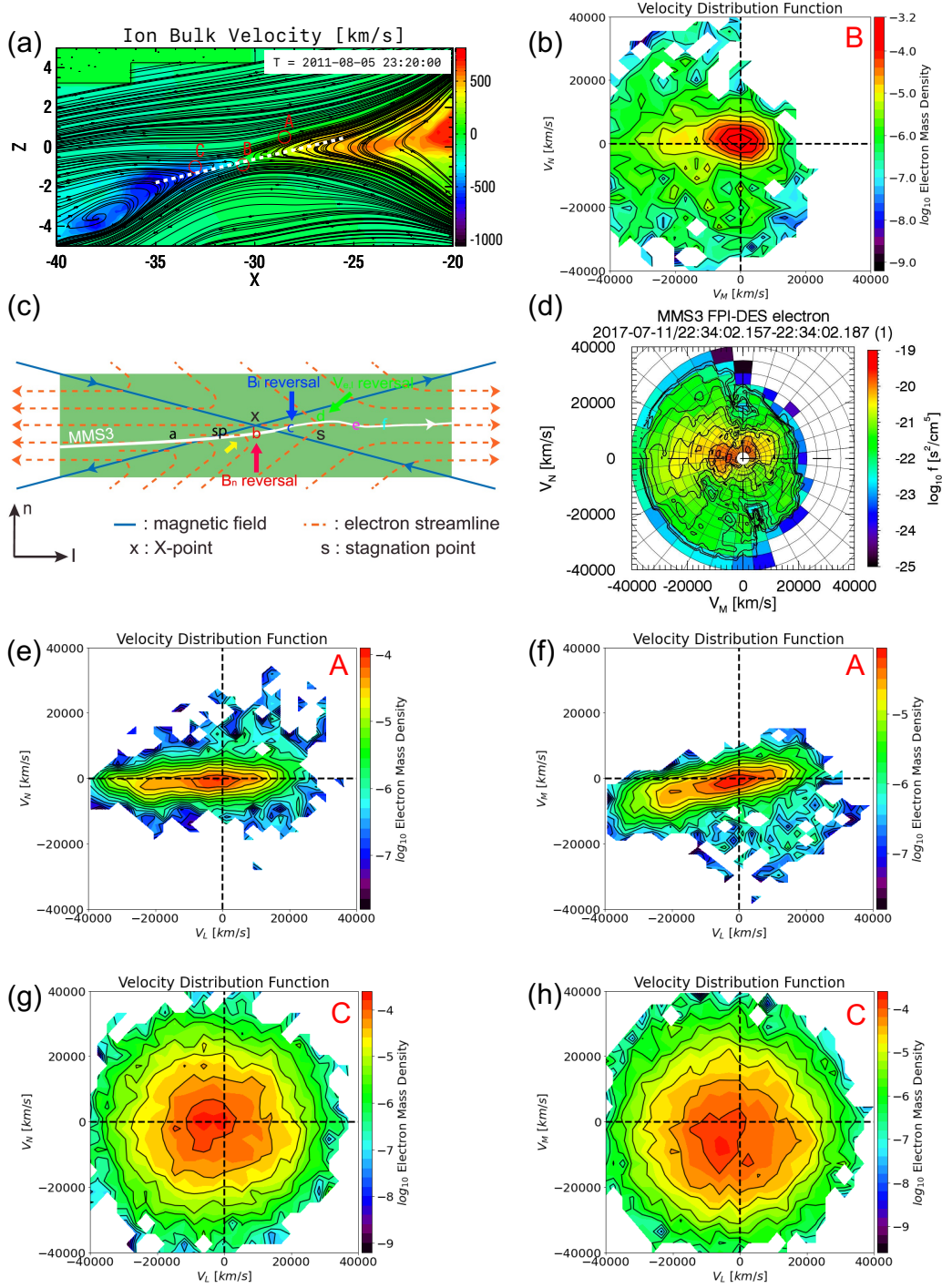


Figure 10. (a) The contour plot of the ion bulk velocity overlapped with magnetic field lines. The 2D cut is taken on the meridional plane. The three red circles are the position where the electrons for the VDF are collected. A: Inflow region, B: Electron Diffusion Region, C: Outflow region. The white dashed line with a Notice that some area at upper left is not covered by PIC which illustrates the AEPIC feature. (b) The electron VDF from the simulation, colored in electron mass density in log scale. (c) A sketch (Figure 1 (b) in Hwang et al. (2019)) demonstrating possible magnetic field geometries. The white curve represents a possible MMS3 trajectory. The electron VDF in (d) is taken at the position *b* pointed by a red arrow. (d) MMS3 observation (Figure 2 (c) in Hwang et al. (2019)). (e)-(f) The electron VDF taken at the inflow region. (g)-(h) The electron VDF taken at the outflow region.

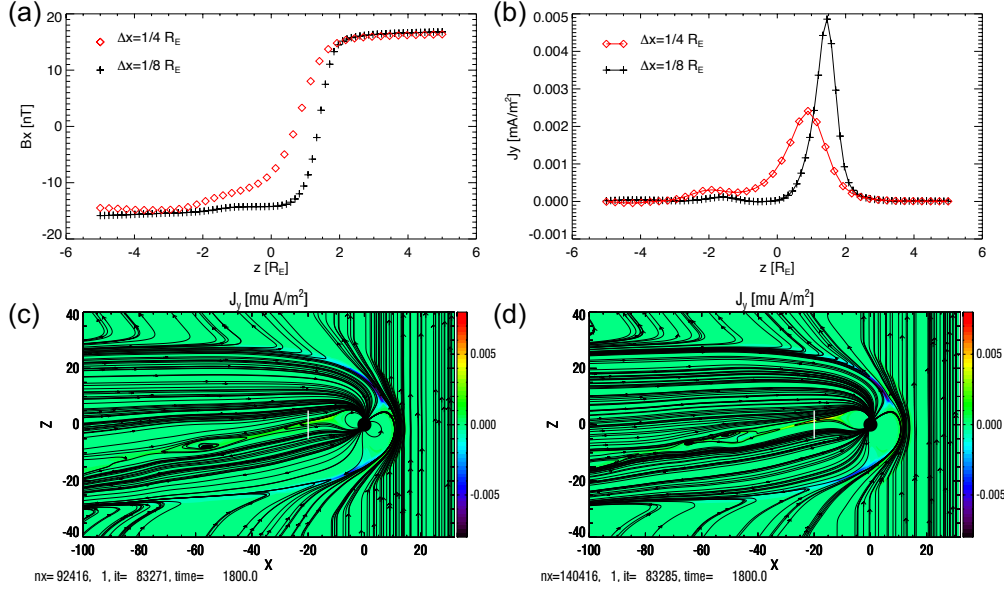


Figure 11. (a) The B_x profiles across the current sheet from two simulations with different grid resolutions in the magnetotail. The profiles are taken along the $x = -20 R_E$ and $y = 0$ line from $z = -5 R_E$ to $5 R_E$. The symbols show the discrete values at the grid cell centers. (b) The J_y current profiles taken at the same position as B_x in panel (a). (c) The meridional cut of the simulation domain with J_y and magnetic field lines for $1/4 R_E$ grid resolution in the magnetotail. (d) Same physical quantities as panel (c) but with $1/8 R_E$ grid resolution in the magnetotail. Two snapshots are taken at the same time 2011-08-05 15:30:00.

672 The main argument is that an ideal MHD reconnecting current sheet behaves like
 673 a discontinuity and therefore the derivatives of the solution across the current sheet
 674 do not converge to a finite value. In particular, the current density, obtained from the deriva-
 675 tive of the magnetic field, goes to infinity as the grid resolution is increased, while the
 676 numerical diffusion goes to zero. Their product, which determines the reconnection rate,
 677 remains finite. Although it is still an open question, the Axford Conjecture (Axford, 1984;
 678 Gonzalez et al., 2016) suggests that the global time averaged reconnection rate is pre-
 679 dominantly set by the external solar wind and IMF driver. On the dayside, the solar wind
 680 brings in magnetic flux at a rate of $|u_x|B_z$. A fraction of this flux will reconnect at the
 681 dayside magnetopause for $B_z < 0$. For a time period that is much longer than substorms,
 682 since the magnetic flux attached to Earth cannot grow without bound, there has to be
 683 a matching reconnection rate in the magnetotail.

684 We now look into more detail, how the numerical scheme actually achieves this. For
 685 finite volume methods solving the

$$\frac{\partial U}{\partial t} + \nabla \cdot F = 0 \quad (\text{A3})$$

686 equation, the numerical flux is calculated at the cell interfaces, and it depends on the
 687 right and left states U^R and U^L extrapolated from the right and left directions, respec-
 688 tively, and the characteristic wave speeds. The Lax-Friedrichs flux is the simplest exam-
 689 ple:

$$F^{LF} = \frac{F(U^R) + F(U^L)}{2} - \frac{1}{2} \lambda_{\max}(U^R - U^L) \quad (\text{A4})$$

690 where F is the physical flux function. The first term contains the physical flux as the av-
 691 erage of $F(U^R)$ and $F(U^L)$. The second term introduces numerical diffusion to preserve

692 the monotonicity of the numerical solution. The numerical diffusion is proportional to
 693 the fastest wave speed λ_{\max} corresponding to the fast magnetosonic wave in ideal MHD.
 694 The $U^R - U^L$ difference is some fraction of the difference between the cell center val-
 695 ues on the two sides of the cell:

$$(U^R - U^L)_f = \alpha_f (U_{k+1} - U_k) \quad (\text{A5})$$

696 Here f represents the index of the cell face between cells indexed by k and $k+1$. The
 697 fraction $0 \leq \alpha_f \leq 1$ depends on the numerical scheme. For a first order scheme $\alpha_f =$
 698 1. For a higher order scheme, the fraction depends on the limiters used in the algorithm
 699 and the differences of U in neighboring cells.

700 For sake of simplicity, let us consider a current sheet parallel to the X - Y plane
 701 and assume that B_x changes sign across the current sheet as we move in the Z direc-
 702 tion. The physical flux function in the Z direction is $F = v_z B_x - v_x B_z$. The numeri-
 703 cal flux function at the cell interface f is

$$F_f^{LF} = \frac{F(U_f^R) + F(U_f^L)}{2} - \frac{1}{2} \lambda_{\max, f} \alpha_f (B_{x, k+1} - B_{x, k}) \quad (\text{A6})$$

704 The numerical diffusive part of the flux can be written as

$$F_f^{\text{diff}} = - \frac{\lambda_{\max, f} \alpha_f \Delta z}{2} \frac{B_{x, k+1} - B_{x, k}}{\Delta z} \quad (\text{A7})$$

705 which is a numerical approximation of $\eta' \partial_z B_x$ with the numerical diffusivity

$$\eta' = \frac{\lambda_{\max, f} \alpha_f \Delta z}{2} \quad (\text{A8})$$

706 Indeed in the 1D case with $\partial_y = \partial_z = 0$, the last term in equation (A2) simplifies to

$$-\nabla \times (\eta' \nabla \times \mathbf{B}) = \frac{\partial}{\partial z} \left(\eta' \frac{\partial \mathbf{B}}{\partial z} \right) \quad (\text{A9})$$

707 which is equivalent with the negative divergence of the numerical flux in (A7).

708 For a smooth solution $\partial_z B_x$ converges to a finite value as the grid is refined, while
 709 η' converges to zero because $\Delta z \rightarrow 0$. For a discontinuous solution, however, the dif-
 710 ference $B_{x, k+1} - B_{x, k}$ as well as $\lambda_{\max, f}$ and α_f all become independent of the grid res-
 711 olution as $\Delta z \rightarrow 0$. This is a direct consequence of the fact that neither the ideal MHD
 712 equations, nor the numerical scheme has any intrinsic length scale other than the grid
 713 cell size. This means that the current sheet will be resolved with a fixed number of grid
 714 points following a fixed numerical profile (a series of the discrete values $B_{x, k}$ across the
 715 current sheet) independent of the grid resolution for small enough Δz . Therefore the nu-
 716 merical reconnection rate will converge to a finite value, determined predominantly by
 717 the external conditions (the external field $B_x^{\pm \text{ext}}$ and the converging velocity $u_z^{\pm \text{ext}}$ out-
 718 side the current sheet), instead of zero. In physical terms, the numerical resistivity η'
 719 goes to 0, but the current density $(1/\mu_0) \Delta B_x / \Delta z$ goes to infinity and their product re-
 720 mains finite.

721 The maximum possible numerical reconnection rate is $\lambda_{\max, f} |B^{+\text{ext}} - B^{-\text{ext}}| / 2$
 722 corresponding to a current sheet where the magnetic field jumps from $B_x^L = B_{x, k} =$
 723 $B_x^{-\text{ext}}$ to $B_x^R = B_{x, k+1} = B_x^{+\text{ext}}$ across a single cell face, and $\lambda_{\max, f}$ is the maximum
 724 (or average) of the fast magnetosonic speeds taken at the two cell centers next to the face.
 725 The fraction α_f is 1 at this interface independent of the nominal order of the scheme,
 726 because all schemes drop to first order at this type of numerical discontinuity due to the
 727 limiters. This maximum numerical reconnection rate far exceeds the typical physical re-
 728 connection rate $\approx 0.1 v_A |B^{\text{ext}}|$, where v_A is the Alfvén speed, found in PIC simulations.
 729 Note that while the 1D reconnection geometry looks like a Sweet-Parker type reconnec-
 730 tion, the numerical resistivity can far exceed the physical collisional resistivity, so it can

731 be fast. The actual numerical profile realized by the numerical scheme will have multi-
 732 ple points across the current sheet resulting in a lower numerical diffusion rate than the
 733 theoretical maximum. In a 2 or 3 dimensional system, the global reconnection rate will
 734 depend on many factors, including the presence of Hall physics, which has a major im-
 735 pact on the structure of the reconnection site (Birn et al., 2001) and the achievable re-
 736 connection rate.

737 Figure 11 shows that these theoretical consideration are indeed valid in a compli-
 738 cated 3D magnetosphere simulation. We have performed two ideal MHD simulations with
 739 $\Delta x = 1/4 R_E$ and $1/8 R_E$ grid resolutions in the magnetotail, respectively. We com-
 740 pare the numerical solution across the current sheet at the same place and same time.
 741 As the figure shows, the number of grid cells, represented by the symbols, across the cur-
 742 rent sheet and the magnetic field values at the cell centers are essentially the same in the
 743 two simulations. The only change is the physical distance between the cells, which is re-
 744 duced by a factor of 2 on the finer grid. As a result, the current density is twice higher,
 745 while the numerical dissipation rate is half of those obtained on the coarser grid. In the
 746 end, the reconnection rate is essentially the same in the two simulations, which results
 747 in essentially the same global solution.

748 References

- 749 Angelopoulos, V., Kennel, C. F., Coroniti, F. V., Pellat, R., Kivelson, M. G.,
 750 Walker, R. J., ... Gosling, J. T. (1994). Statistical characteristics of bursty
 751 bulk flow events. *J. Geophys. Res.*, *99*, 21,257.
- 752 Asano, Y., Nakamura, R., Shinohara, I., Fujimoto, M., Takada, T., Baumjohann,
 753 W., ... others (2008). Electron flat-top distributions around the magnetic re-
 754 connection region. *Journal of Geophysical Research: Space Physics*, *113*(A1).
- 755 Aunai, N., Hesse, M., & Kuznetsova, M. (2013). Electron nongyrotropy in the con-
 756 text of collisionless magnetic reconnection. *Physics of Plasmas*, *20*(9), 092903.
- 757 Axford, W. (1984). Magnetic field reconnection. *Washington DC American Geophys-*
 758 *ical Union Geophysical Monograph Series*, *30*, 1–8.
- 759 Bergin, A., Chapman, S. C., & Gjerloev, J. W. (2020). Ae, dst, and their supermag
 760 counterparts: The effect of improved spatial resolution in geomagnetic indices.
 761 *Journal of Geophysical Research: Space Physics*, *125*(5), e2020JA027828.
- 762 Birn, J., Drake, J. F., Shay, M. A., Rogers, B. N., Denton, R. E., Hesse, M., ...
 763 Pritchett, P. L. (2001). Geospace Environmental Modeling (GEM) mag-
 764 netic reconnection challenge. *J. Geophys. Res.*, *106*(A3), 3715–3720. doi:
 765 10.1029/1999JA900449
- 766 Birn, J., Hesse, M., & Schindler, K. (2006). Entropy conservation in simulations of
 767 magnetic reconnection. *Physics of plasmas*, *13*(9), 092117.
- 768 Birn, J., Hesse, M., Schindler, K., & Zaharia, S. (2009). Role of entropy in magneto-
 769 tail dynamics. *Journal of Geophysical Research: Space Physics*, *114*(A9).
- 770 Brecht, S., Lyon, J., Fedder, J., & Hain, K. (1981). A simulation study of east-west
 771 IMF effects on the magnetosphere. *Geophys. Res. Lett.*, *8*, 397–400.
- 772 Brecht, S., Lyon, J., Fedder, J., & Hain, K. (1982). A time-dependent three-
 773 dimensional simulation of the earth’s magnetosphere: Reconnection events.
 774 *J. Geophys. Res.*, *87*, 6098–6108.
- 775 Burch, J. L., Torbert, R. B., Phan, T. D., Chen, L.-J., Moore, T. E., Ergun, R. E.,
 776 ... Chandler, M. (2016). Electron-scale measurements of magnetic reconnec-
 777 tion in space. *Science*, *352*, 6290. doi: 10.1126/science.aaf2939
- 778 Chen, L.-J., Hesse, M., Wang, S., Gershman, D., Ergun, R., Pollock, C., ... others
 779 (2016). Electron energization and mixing observed by mms in the vicinity of
 780 an electron diffusion region during magnetopause reconnection. *Geophysical*
 781 *Research Letters*, *43*(12), 6036–6043.
- 782 Chen, Y., & Tóth, G. (2019). Gauss’s law satisfying energy-conserving semi-implicit

- 783 particle-in-cell method. *J. Comput. Phys.*, *386*, 632. doi: 10.1016/j.jcp.2019.02
784 .032
- 785 Chen, Y., Tóth, G., Cassak, P., Jia, X., Gombosi, T. I., Slavin, J., . . . Peng,
786 B. (2017). Global three-dimensional simulation of earth’s dayside recon-
787 nection using a two-way coupled magnetohydrodynamics with embedded
788 particle-in-cell model: initial results. *J. Geophys. Res.*, *122*, 10318. doi:
789 10.1002/2017JA024186
- 790 Chen, Y., Toth, G., Zhou, H., & Wang, X. (2021). Fleks: A flexible particle-in-
791 cell code for multi-scale plasma simulations. *Earth and Space Science Open*
792 *Archive*. doi: doi.org/10.1002/essoar.10508070.1
- 793 Chen, Y., Tóth, G., Jia, X., Slavin, J. A., Sun, W., Markidis, S., . . . Raines, J. M.
794 (2019). Studying dawn-dusk asymmetries of mercury’s magnetotail using mhd-
795 epic simulations. *Journal of Geophysical Research: Space Physics*, *124* (11),
796 8954-8973.
- 797 Daldorff, L. K. S., Tóth, G., Gombosi, T. I., Lapenta, G., Amaya, J., Markidis, S., &
798 Brackbill, J. U. (2014). Two-way coupling of a global Hall magnetohydrody-
799 namics model with a local implicit Particle-in-Cell model. *J. Comput. Phys.*,
800 *268*, 236. doi: 10.1016/j.jcp.2014.03.009
- 801 Daughton, W., Scudder, J., & Karimabadi, H. (2006). Fully kinetic simulations
802 of undriven magnetic reconnection with open boundary conditions. *Physics of*
803 *Plasmas*, *13*(7), 072101.
- 804 Davis, T. N., & Sugiura, M. (1966). Auroral electrojet activity index *ae* and its uni-
805 versal time variations. *Journal of Geophysical Research*, *71*(3), 785–801.
- 806 De Zeeuw, D., Sazykin, S., Wolf, R., Gombosi, T., Ridley, A., & Tóth, G. (2004).
807 Coupling of a global MHD code and an inner magnetosphere model: Initial
808 results. *J. Geophys. Res.*, *109*(A12), 219. doi: 10.1029/2003JA010366
- 809 Dedner, A., Kemm, F., Kröner, D., Munz, C., Schnitzer, T., & Wesenberg, M.
810 (2003). Hyperbolic divergence cleaning for the MHD equations. *J. Comput.*
811 *Phys.*, *175*, 645–673.
- 812 Egedal, J., Lê, A., Katz, N., Chen, L.-J., Lefebvre, B., Daughton, W., & Fazakerley,
813 A. (2010). Cluster observations of bidirectional beams caused by electron
814 trapping during antiparallel reconnection. *Journal of Geophysical Research:*
815 *Space Physics*, *115*(A3).
- 816 Ganushkina, N., Jaynes, A., & Liemohn, M. (2017). Space weather effects produced
817 by the ring current particles. *Space Science Reviews*, *212*(3), 1315–1344.
- 818 Gao, Y. (2012). Comparing the cross polar cap potentials measured by superdarn
819 and amie during saturation intervals. *Journal of Geophysical Research: Space*
820 *Physics*, *117*(A8).
- 821 Glocer, A., Dorelli, J., Tóth, G., Komar, C. M., & Cassak, P. A. (2016). Sepa-
822 rator reconnection at the magnetopause for predominantly northward and
823 southward IMF: techniques and results. *J. Geophys. Res.*, *120*, 5377. doi:
824 10.1002/2015JA021417
- 825 Glocer, A., Tóth, G., Ma, Y. J., Gombosi, T., Zhang, J.-C., & Kistler, L. M. (2009).
826 Multifluid Block-Adaptive-Tree Solar wind Roe-type Upwind Scheme: Mag-
827 netospheric composition and dynamics during geomagnetic storms – initial
828 results. *J. Geophys. Res.*, *114*, A12203. doi: 10.1029/2009JA014418
- 829 Gonzalez, W., Parker, E., Mozer, F., Vasyliūnas, V., Pritchett, P., Karimabadi, H.,
830 . . . others (2016). Fundamental concepts associated with magnetic reconnec-
831 tion. In *Magnetic reconnection* (pp. 1–32). Springer.
- 832 Haiducek, J. D., Welling, D. T., Ganushkina, N. Y., Morley, S. K., & Ozturk, D. S.
833 (2017). Swmf global magnetosphere simulations of january 2005: Geomagnetic
834 indices and cross-polar cap potential. *Space Weather*, *15*(12), 1567–1587.
- 835 Hairston, M. R., Weimer, D. R., Heelis, R. A., & Rich, F. (1998). Analysis of the
836 ionospheric cross polar cap potential drop and electrostatic potential distribu-
837 tion patterns during the January 1997 CME event using DMSP data. *JATP*,

- 838 61, 195–206.
- 839 Hones Jr, E., Birn, J., Baker, D., Bame, S., Feldman, W., McComas, D., . . . Tsuru-
840 tani, B. (1984). Detailed examination of a plasmoid in the distant magnetotail
841 with isee 3. *Geophysical research letters*, 11(10), 1046–1049.
- 842 Hwang, K.-J., Choi, E., Dokgo, K., Burch, J., Sibeck, D., Giles, B., . . . others
843 (2019). Electron vorticity indicative of the electron diffusion region of mag-
844 netic reconnection. *Geophysical research letters*, 46(12), 6287–6296.
- 845 Janhunen, P. (1996). GUMICS-3: A global ionosphere-magnetosphere coupling
846 simulation with high ionospheric resolution. In *Proceedings of the ESA 1996*
847 *symposium on environment modelling for space-based applications* (pp. 233–
848 239). ESA SP-392.
- 849 Koren, B. (1993). A robust upwind discretisation method for advection, diffusion
850 and source terms. In C. Vreugdenhil & B.Koren (Eds.), *Numerical methods for*
851 *advection-diffusion problems* (p. 117). Vieweg, Braunschweig.
- 852 LeBoeuf, J. N., Tajima, T., Kennel, C. F., & Dawson, J. M. (1981). Global sim-
853 ulations of the three-dimensional magnetosphere. *Geophys. Res. Lett.*, 8, 257–
854 260.
- 855 Li, X., Guo, F., & Li, H. (2019). Particle acceleration in kinetic simulations of non-
856 relativistic magnetic reconnection with different ion–electron mass ratios. *The*
857 *Astrophysical Journal*, 879(1), 5.
- 858 Lotekar, A., Vasko, I., Mozer, F., Hutchinson, I., Artemyev, A., Bale, S., . . . others
859 (2020). Multisatellite mms analysis of electron holes in the earth’s magneto-
860 tail: Origin, properties, velocity gap, and transverse instability. *Journal of*
861 *Geophysical Research: Space Physics*, 125(9), e2020JA028066.
- 862 Lyon, J., Fedder, J., & Mobarry, C. (2004). The Lyon-Fedder-Mobarry (LFM) global
863 MHD magnetospheric simulation code. *J. Atmos. Sol-Terr. Phys.*, 66, 1333.
- 864 Lyon, J. G., Fedder, J., & Huba, J. (1986). The effect of different resistivity models
865 on magnetotail dynamics. *J. Geophys. Res.*, 91, 8057–8064.
- 866 Ma, X., & Otto, A. (2014). Nonadiabatic heating in magnetic reconnection. *Journal*
867 *of Geophysical Research: Space Physics*, 119(7), 5575–5588.
- 868 Ma, Y., Russell, C. T., Toth, G., Chen, Y., Nagy, A. F., Harada, Y., . . . others
869 (2018). Reconnection in the martian magnetotail: Hall-mhd with embedded
870 particle-in-cell simulations. *Journal of Geophysical Research: Space Physics*,
871 123(5), 3742–3763.
- 872 Markidis, S., Henri, P., Lapenta, G., Divin, A., Goldman, M., Newman, D., & Laure,
873 E. (2013). Kinetic simulations of plasmoid chain dynamics. *Physics of Plas-*
874 *mas*, 20(8), 082105.
- 875 Markidis, S., Lapenta, G., & Rizwan-Uddin. (2010). Multi-scale simulations of
876 plasma with ipic3d. *Mathematics and Computers in Simulation*, 80, 1509–
877 1519. doi: 10.1016/j.matcom.2009.08.038
- 878 Merkin, V. G., Panov, E. V., Sorathia, K., & Ukhorskiy, A. Y. (2019). Contribution
879 of bursty bulk flows to the global dipolarization of the magnetotail during an
880 isolated substorm. *Journal of Geophysical Research: Space Physics*, 124(11),
881 8647–8668.
- 882 Newell, P., & Gjerloev, J. (2011). Evaluation of supermag auroral electrojet indices
883 as indicators of substorms and auroral power. *Journal of Geophysical Research:*
884 *Space Physics*, 116(A12).
- 885 Powell, K., Roe, P., Linde, T., Gombosi, T., & De Zeeuw, D. L. (1999). A solution-
886 adaptive upwind scheme for ideal magnetohydrodynamics. *J. Comput. Phys.*,
887 154, 284–309. doi: 10.1006/jcph.1999.6299
- 888 Pritchett, P. (2006). Relativistic electron production during driven magnetic recon-
889 nection. *Geophysical research letters*, 33(13).
- 890 Pulkkinen, A., Rastatter, L., Kuznetova, M., Singer, H., Balch, C., Weimer, D., . . .
891 Weigel, R. (2013). Community-wide validation of geospace model ground mag-
892 netic field perturbation predictions to support model transition to operations.

- 893 *Space Weather*, 11, 369–385. doi: 10.1002/swe.20056
- 894 Raeder, J., Berchem, J., & Ashour-Abdalla, M. (1996). The importance of small
895 scale processes in global MHD simulations: Some numerical experiments. In
896 T. Chang & J. R. Jasperse (Eds.), *The physics of space plasmas* (Vol. 14,
897 p. 403). Cambridge, Mass..
- 898 Raeder, J., McPherron, R., Frank, L., Kokubun, S., Lu, G., Mukai, T., ... Slavin,
899 J. (2001). Global simulation of the Geospace Environment Modeling substorm
900 challenge event. *J. Geophys. Res.*, 106, 281.
- 901 Raeder, J., Walker, R. J., & Ashour-Abdalla, M. (1995). The structure of the dis-
902 tant geomagnetic tail during long periods of northward IMF. *Geophys. Res.*
903 *Lett.*, 22, 349–352.
- 904 Richmond, A., & Kamide, Y. (1988). Mapping electrodynamic features of the high-
905 latitude ionosphere from localized observations: Technique. *J. Geophys. Res.*,
906 93, 5741–5759.
- 907 Ridley, A., Gombosi, T., & Dezeew, D. (2004, February). Ionospheric control of the
908 magnetosphere: conductance. *Annales Geophysicae*, 22, 567–584. doi: 10.5194/
909 angeo-22-567-2004
- 910 Ridley, A. J., & Kihn, E. A. (2004, Apr). Polar cap index comparisons with AMIE
911 cross polar cap potential, electric field, and polar cap area. *Geophysical Re-*
912 *search Letters*, 31, 07801. doi: 10.1029/2003GL019113
- 913 Ruohoniemi, J., & Greenwald, R. (1998). The response of high latitude convection
914 to a sudden southward IMF turning. *Geophys. Res. Lett.*, 25, 2913.
- 915 Schindler, K. (1974). A theory of the substorm mechanism. *Journal of Geophysical*
916 *Research*, 79(19), 2803–2810.
- 917 Shou, Y., Tenishev, V., Chen, Y., Toth, G., & Ganushkina, N. (2021). Magneto-
918 hydrodynamic with adaptively embedded particle-in-cell model: Mhd-aepic.
919 *Journal of Computational Physics*, 110656.
- 920 Slavin, J., Baker, D., Craven, J., Elphic, R., Fairfield, D., Frank, L., ... others
921 (1989). Cdaw 8 observations of plasmoid signatures in the geomagnetic tail:
922 An assessment. *Journal of Geophysical Research: Space Physics*, 94(A11),
923 15153–15175.
- 924 Slavin, J., Lepping, R., Gjerloev, J., Fairfield, D., Hesse, M., Owen, C., ... Mukai,
925 T. (2003). Geotail observations of magnetic flux ropes in the plasma sheet.
926 *Journal of Geophysical Research: Space Physics*, 108(A1), SMP–10.
- 927 Sokolov, I. V., Timofeev, E. V., Sakai, J. I., & Takayama, K. (1999). On shock cap-
928 turing schemes using artificial wind. *Shock Waves*, 9, 423–426.
- 929 Toffoletto, F., Sazykin, S., Spiro, R., & Wolf, R. (2003). Inner magnetospheric mod-
930 eling with the Rice Convection Model. *Space Sci. Rev.*, 107, 175–196. doi: 10
931 .1023/A:1025532008047
- 932 Torbert, R., Burch, J., Phan, T., Hesse, M., Argall, M., Shuster, J., ... others
933 (2018). Electron-scale dynamics of symmetric magnetic reconnection diffu-
934 sion region in space. *Science*, 362(6421), 1391–1395.
- 935 Tóth, G., Chen, Y., Gombosi, T. I., Cassak, P., , Markidis, S., & Peng, B. (2017).
936 Scaling the ion inertial length and its implications for modeling reconnection in
937 global simulations. *J. Geophys. Res.*, 122, 10336. doi: 10.1002/2017JA024189
- 938 Tóth, G., Jia, X., Markidis, S., Peng, B., Chen, Y., Daldorff, L., ... Dorelli, J.
939 (2016). Extended magnetohydrodynamics with embedded particle-in-cell
940 simulation of ganymede’s magnetosphere. *J. Geophys. Res.*, 121. doi:
941 10.1002/2015JA021997
- 942 Tóth, G., Ma, Y. J., & Gombosi, T. I. (2008). Hall magnetohydrodynamics on block
943 adaptive grids. *J. Comput. Phys.*, 227, 6967–6984. doi: 10.1016/j.jcp.2008.04
944 .010
- 945 Tóth, G., van der Holst, B., Sokolov, I. V., Zeeuw, D. L. D., Gombosi, T. I., Fang,
946 F., ... Opher, M. (2012). Adaptive numerical algorithms in space weather
947 modeling. *J. Comput. Phys.*, 231, 870–903. doi: 10.1016/j.jcp.2011.02.006

- 948 Tóth, G., Zeeuw, D. L. D., Gombosi, T. I., Manchester, W. B., Ridley, A. J.,
949 Sokolov, I. V., & Roussev, I. I. (2007). Sun to thermosphere simulation of
950 the October 28-30, 2003 storm with the Space Weather Modeling Framework.
951 *Space Weather Journal*, 5, S06003. doi: 10.1029/2006SW000272
- 952 Troshichev, O., Andezen, V., Vennerstrom, S., & Friis-Cristensen, E. (1988). Mag-
953 netic activity in the polar cap - a new index. *Planet. Space. Sci.*, 36, 1095.
- 954 Troshichev, O., Hayakawa, H., Matsuoka, A., Mukai, T., & Tsuruda, K. (1996).
955 Cross polar cap diameter and voltage as a function of *PC* index and interplane-
956 tary quantities. *J. Geophys. Res.*, 101, 13,429.
- 957 Tsutomu, T., & Teruki, M. (1976). Flapping motions of the tail plasma sheet in-
958 duced by the interplanetary magnetic field variations. *Planetary and Space Sci-*
959 *ence*, 24(2), 147–159.
- 960 Volwerk, M., Andre, N., Arridge, C., Jackman, C., Jia, X., Milan, S. E., . . . others
961 (2013). Comparative magnetotail flapping: An overview of selected events at
962 earth, jupiter and saturn. In *Annales geophysicae* (Vol. 31, pp. 817–833).
- 963 Webster, J., Burch, J., Reiff, P., Daou, A., Genestreti, K., Graham, D. B., . . . oth-
964 ers (2018). Magnetospheric multiscale dayside reconnection electron diffusion
965 region events. *Journal of Geophysical Research: Space Physics*, 123(6), 4858–
966 4878.
- 967 Wiltberger, M., Merkin, V., Lyon, J., & Ohtani, S. (2015). High-resolution global
968 magnetohydrodynamic simulation of bursty bulk flows. *Journal of Geophysical*
969 *Research: Space Physics*, 120(6), 4555–4566.
- 970 Wolf, R. A., Harel, M., Spiro, R. W., Voigt, G., Reiff, P. H., & Chen, C. K.
971 (1982). Computer simulation of inner magnetospheric dynamics for the
972 magnetic storm of July 29, 1977. *J. Geophys. Res.*, 87, 5949-5962. doi:
973 10.1029/JA087iA08p05949
- 974 Wu, C. C., Walker, R., & Dawson, J. M. (1981). A three-dimensional MHD model of
975 the Earth’s magnetosphere. *Geophys. Res. Lett.*, 8, 523–526.
- 976 Zhou, H., Tóth, G., Jia, X., & Chen, Y. (2020). Reconnection-driven dynam-
977 ics at ganymede’s upstream magnetosphere: 3-d global hall mhd and mhd-
978 epic simulations. *Journal of Geophysical Research: Space Physics*, 125(8),
979 e2020JA028162.
- 980 Zhou, H., Tóth, G., Jia, X., Chen, Y., & Markidis, S. (2019). Embedded kinetic sim-
981 ulation of ganymede’s magnetosphere: Improvements and inferences. *Journal*
982 *of Geophysical Research: Space Physics*, 124(7), 5441–5460.